

# IMPROVING THE PROTEIN PIPELINE THROUGH NONLINEAR OPTICAL METHODS

by

**Hilary M. Florian**

**A Dissertation**

*Submitted to the Faculty of Purdue University*

*In Partial Fulfillment of the Requirements for the degree of*

**Doctor of Philosophy**



Department of Chemistry

West Lafayette, Indiana

August 2020

**THE PURDUE UNIVERSITY GRADUATE SCHOOL**  
**STATEMENT OF COMMITTEE APPROVAL**

**Dr. Garth Simpson, Chair**

Department of Chemistry

**Dr. Chittaranjan Das**

Department of Chemistry

**Dr. Mary Wirth**

Department of Chemistry

**Dr. Adam Wasserman**

Department of Chemistry

**Approved by:**

Dr. Christine Hrycyna

*To my grandfather, I hope you'd be proud of me*

## ACKNOWLEDGMENTS

First, I would like to thank the many mentors who have helped me during my graduate career. Garth, thank you for creating a research environment that not only drives exciting science but also facilitates collaboration and friendship. Marybeth, thank you for making me into the instructor I am today. Your constant support and patience for my never-ending questions led to me choosing education for my future career. I am forever grateful for your encouragement, friendship, and guidance. Also, thank you to the team at Argonne, especially Michael Becker and David Kissick. My time at Argonne has helped shape me into the scientist I am today and that would not be possible without your help.

Thank you to the many friends I have made while at Purdue. Alex, words can't begin to cover how much I appreciate you and your friendship. You have been there through some of the hardest times in my life and have always been there to offer support, whether that be going to lunch to get out of the office, going to concerts, drag shows, and bars together, complaining about Duolingo together, or joining in on my self-deprecating humor. You're irreplaceable and I hope we continue to be friends for life! Nita, we've only known each other for a couple of years, but in that time, you have become one of my closest friends. I don't know how I would have gotten through this without your support and friendship. James, thanks for keeping me grounded during many bouts of anxiety and reminding me that things are never as bad as I think. Scott, thank you not just for being the best dog sitter, but also for always being there to vent to, for being willing to go to any movie I wanted to see, and just for being one of the best friends I could ask for. And thank you to the rest of the Simpson lab, as we all know, Simpson lab best lab!

And of course, thanks to my family, who despite their hesitancy towards me moving six hours away, have constantly supported me during my pursuit in higher education. To my parents, for allowing me to believe I could accomplish anything I set my mind to, and especially my mom, for tolerating my many calls stressing out about being an adult. To my brother, Matthew, for being the only family member to somewhat understand my crazy decision to go to grad school and the stress that came with that decision. Also, thank you for always providing comic relief that has gotten me through many difficult times. Grandma and Aunt Patty, thank you for the love and support you always provide. Natalie, thanks for always being up to discussing what happened

during Grey's Anatomy! And thank you to Emma and Lucas, for always being able to put a smile on my face.

Last but certainly not least, thank you to my loving boyfriend Ben, for being there for me through all the stress and anxiety caused by finishing my PhD. Thank you for making me breakfast on the weekends, for playing board games with me, for supporting my book addiction, for encouraging me, and for keeping me sane during quarantine. I'm grateful and excited to start the next phase of my life with you by my side!

## TABLE OF CONTENTS

LIST OF TABLES .....	10
LIST OF FIGURES .....	11
LIST OF ABBREVIATIONS .....	14
ABSTRACT.....	16
CHAPTER 1. INTRODUCTION .....	18
1.1 The role of the protein pipeline in rational drug design.....	18
1.2 Challenges and advances in protein detection and characterization .....	19
1.3 Nonlinear optical imaging techniques .....	20
1.4 Dissertation overview .....	23
1.5 References.....	25
CHAPTER 2. NON-NEGATIVE MATRIX FACTORIZATION FOR ISOLATING DAMAGE-FREE REFLECTIONS IN MACROMOLECULAR SYNCHROTRON DATA COLLECTION .....	27
2.1 Introduction.....	27
2.2 Methods.....	28
2.2.1 Sample preparation .....	28
2.2.2 XRD data collection .....	29
2.2.3 Dimension reduction of XRD data .....	30
2.2.4 Non-negative matrix factorization (NMF).....	31
2.2.5 Kinetic modeling .....	31
2.3 Results and discussion .....	32
2.3.1 NMF decomposition of cryogenic lysozyme XRD .....	32
2.3.2 Kinetic analysis of NMF components .....	33
2.3.3 NMF decomposition of room-temperature lysozyme XRD .....	35
2.3.4 Discussion.....	36
2.4 Conclusion .....	39
2.5 References.....	39
CHAPTER 3. MODIFICATIONS TO A MULTIMODAL NONLINEAR OPTICAL MICROSCOPE INSTALLED AT A SYNCHROTRON.....	44

3.1	Introduction.....	44
3.2	Methods.....	46
3.2.1	Beam path modifications .....	46
3.2.2	Design of custom objective .....	47
3.2.3	Data acquisition .....	48
3.3	Results and discussion .....	48
3.3.1	Discussion of modifications .....	48
3.3.2	Testing the custom objective .....	49
3.4	Conclusion and future work.....	51
3.5	References.....	52
CHAPTER 4. DEPTH OF FIELD EXTENSION FOR HIGH THROUGHPUT CRYSTAL SCREENING USING A CUSTOM MICRORETARDER ARRAY .....		54
4.1	Introduction.....	54
4.2	Methods.....	55
4.2.1	BaTiO <sub>3</sub> sample preparation.....	55
4.2.2	Ritonavir crystal growth .....	56
4.2.3	Crystallization and preparation of tetragonal lysozyme .....	56
4.2.4	SHG measurements .....	56
4.3	Results.....	57
4.3.1	Imaging of BaTiO <sub>3</sub> nanoparticles .....	57
4.3.2	Imaging of ritonavir crystals.....	58
4.3.3	Imaging of tetragonal lysozyme crystals .....	59
4.3.4	High-throughput crystal screening .....	60
4.4	Conclusions.....	61
4.5	References.....	62
CHAPTER 5. POLARIZATION DEPENDENT IMAGING USING A MICRORETARDER ARRAY FOR DISCRIMINATION BETWEEN CRYSTALLINE AND AGGREGATE PROTEINS .....		64
5.1	Introduction.....	64
5.2	Theoretical framework.....	66
5.2.1	Polarization analysis for TPE-UVF .....	66

5.3	Methods.....	69
5.3.1	Sample preparation .....	69
5.3.2	Data acquisition .....	69
5.3.3	Data analysis .....	70
5.4	Results and discussion .....	71
5.5	Conclusions and future work .....	72
5.6	References .....	73
CHAPTER 6. RECOVERY OF SHG SIGNAL AFTER PHOTBLEACHING OF R6G-LABELED LYSOZYME.....		74
6.1	Introduction.....	74
6.2	Methods.....	75
6.2.1	Sample preparation .....	75
6.2.2	Electronics modifications .....	75
6.2.3	Photobleaching .....	76
6.2.4	Temperature ramp and image acquisition.....	76
6.2.5	Data processing.....	77
6.3	Results and discussion .....	77
6.3.1	Photobleaching of lysozyme.....	77
6.3.2	Recovery of SHG intensity as a function of temperature .....	78
6.4	Conclusions and future work .....	79
6.5	References .....	80
CHAPTER 7. SHG ENHANCEMENT IN PROTEIN CRYSTALS USING A TETRACYSSTEINE-FLASH TAG IN MALTOSE BINDING PROTEIN .....		83
7.1	Introduction.....	83
7.2	Methods.....	85
7.2.1	Expression and crystallization of MBP .....	85
7.2.2	Labeling with FlAsH dye.....	85
7.2.3	Fluorimetry measurements .....	85
7.2.4	Acquisition of SHG images .....	85
7.3	Results and discussion .....	86
7.3.1	Fluorescence studies .....	86



7.3.2	Kinetic studies of dye binding .....	87
7.3.3	SHG imaging results.....	87
7.4	Conclusions.....	88
7.5	References.....	88
VITA	.....	90

## LIST OF TABLES

Table 3.1 Specifications of lenses in the custom-built objective.....	48
Table 3.2 Power readings measured at the sample plane with the custom-built objective and Optem objective installed in the system. ....	50
Table 4.1 Comparison of the number of crystal counts detected using the extended DoF method and the conventional SHG imaging method. ....	61
Table 5.1 Results of the Fourier transform of images acquired of tryptophan solution, calculating the ratio of circular to linear polarized light. ....	72

## LIST OF FIGURES

Figure 1.1 Protein structure determination pipeline. ....	19
Figure 1.2 Energy diagram for second harmonic generation.....	21
Figure 1.3 Energy diagram for two-photon excited UV fluorescence.....	22
Figure 1.4 Multimodal crystal detection of an ABC maltose transporter protein; (a) bright field, (b) SHG, (c) and (d) TPE-UVF at 3 min and 3 sec acquisition time, respectively. Figure adapted from Madden et al, 2011. <sup>15</sup> .....	22
Figure 2.1 Schematic of the method used for data acquisition of room temperature XRD of lysozyme crystals, with images showing the area selected for radiation. Crystals were irradiated at one point for five, 10 ms periods initially, then the surrounding mother liquor was irradiated for 1 s followed by a 10 ms exposure at the original point on the crystal for five cycles. ....	29
Figure 2.2 Decomposition of XRD peaks into NMF components. I) Initial XRD pattern of tetragonal lysozyme prior to decomposition. II) Components A-C generated from NMF decomposition of the original XRD pattern. Kinetic modeling revealed a sequential progression from A → B → C with increasing X-ray dose. These XRD patterns show a decrease in diffraction peak intensities in components B and C arising following X-ray exposure. ....	33
Figure 2.3 Kinetics of propagation of damage with X-ray dose in tetragonal lysozyme. Fitting to a kinetic model revealed a sequential progression from A → B → C with increasing X-ray dose. Recovered rate constants from the fit were: $k_{AB} = 0.265 \pm 0.008$ , $k_{AC} = 0.000 \pm 0.008$ , $k_{AD} = 0.00 \pm 0.01$ , $k_{BC} = 0.050 \pm 0.006$ , $k_{BD} = 0.072 \pm 0.007$ , and $k_{CD} = 0.013 \pm 0.003$ , all in units of MGy <sup>-1</sup> . Reported error is the standard deviation of the fit. ....	34
Figure 2.4 NMF analysis of indirect radiation damage to tetragonal lysozyme at room temperature. The vertical lines on the x-axis signify the point at which the X-ray radiation was applied to the region surrounding the crystal. I) The overall integrated intensity of the XRD peaks changes slightly due to damage induced by radiation around the crystal. II) NMF decomposition of the original XRD pattern into three components elucidates the significant change in composition as a function of radiation damage. Dashed lines are a visual aid and do not indicate continuity.....	36
Figure 3.1 Schematic of the original beam path design of the nonlinear optical microscope installed at the beamline 23-ID-B at Argonne National Lab; BF, raster scan, and SHG images of lysozyme are shown to demonstrate how SHG can be used for crystal positioning. Adapted from Madden et al, 2013.....	46
Figure 3.2 Schematic of the beam path before and after redesign. Note, scan head was not moved in the beam path, just for purposes of depicting the schematic. ....	47
Figure 3.3 Schematic of custom-built objective, consisting of 8 lenses with varying focal lengths. ....	48

Figure 3.4 Bright field (a,b) and SHG (c,d) images of BaTiO <sub>3</sub> using both the standard Optem objective (a,c) and the custom built objective (b,d). Note, red circles are used to point out the faint particles visible in the SHG image using the Optem objective. ....	51
Figure 4.1 a) Custom designed pattern of $\mu$ RA for depth of field extension using 1064 nm light. b) Schematic depicting the principle of depth of field extension by polarization wavefront shaping, where arrows indicate different polarization states of light. ....	57
Figure 4.2 a-d) SHG images of BaTiO <sub>3</sub> nanoparticles at different z-planes. e) Summation of SHG images in (a-d). f) Single SHG image of BaTiO <sub>3</sub> nanoparticles with the $\mu$ RA in the beam path, depicting the same field-of-view as shown in (a-d). ....	58
Figure 4.3 A series of SHG images of ritonavir crystals depicting a) the z-projection of images acquired through a z-scan, b) a single image of the same crystals and field-of-view acquired with the $\mu$ RA in place and c) an overlay of the two to show the differences detected by the two methods. ....	59
Figure 4.4 a-c) SHG images of tetragonal lysozyme crystals with intercalated malachite green dye at different z-planes d) Z-projection of SHG images shown in (a-c). e-f) SHG images of the same sample and same field-of-view with the same exposure time (e) and double exposure time (f)..	60
Figure 5.1 Pattern of the microretarder array from Thorlabs; color scale shows the polarization angle across the optic. ....	66
Figure 5.2 Schematic of the beam path for epi TPE-UVF with a $\mu$ RA installed in the rear conjugate plane. ....	70
Figure 5.3 TPE-UVF images of tryptophan solution, tryptophan crystals, and lyophilized lysozyme without and with the $\mu$ RA installed in the beam path. ....	71
Figure 5.4 Fourier transform of tryptophan solution image, with the first and second harmonic peaks circled in red and green, respectively. ....	72
Figure 6.1 Software interface for patterned bleaching using the galvanometer mirror .....	76
Figure 6.2 Profile plot from SHG image of R6G-labeled lysozyme at 100 K, after photobleaching, for measurement of bleach “depth”. ....	77
Figure 6.3 SHG images of R6G-labeled and R6G-intercalated lysozyme crystals pre- and post-bleaching, with red arrows shown to point out the striped pattern post bleach. ....	78
Figure 6.4 SHG recovery after photobleaching of R6G-labeled and R6G-intercalated lysozyme. The temperature of the cryo-stream was increased in 10 K increments and SHG images were acquired after each temperature ramp. The resulting SHG signal recovery is plotted as the normalized depth of bleached stripes vs the temperature of the cryo-stream. ....	79
Figure 7.1 Mechanism of FIAsh dye binding to a tetracysteine tag incorporated into the target protein. ....	84
Figure 7.2 Fluorescence studies of maltose binding protein. After addition of the FIAsh dye, the fluorescence intensity of MBP increased 5-fold, with little fluorescence observed prior to addition	

of the dye. Note that traces for the protein buffer and MBP alone overlap, both are indeed present in the plot. ....	86
Figure 7.3 Kinetic studies of FAsH dye binding to a tetracysteine tag in MBP.....	87
Figure 7.4 SHG images of MBP crystals before (a) and after (b) addition of 500 nM FAsH dye. ....	88

## LIST OF ABBREVIATIONS

APS	Advanced Photon Source
ASD	amorphous solid dispersion
BaTiO <sub>3</sub>	barium titanate
BF	bright field
CBF	Crystallographic Binary File
DoF	depth of field
DCM	dichroic mirror
EOM	electro-optic modulator
FoV	field of view
FRAP	fluorescence recovery after photobleaching
GM/CA@APS	General Medicine and Cancer at Advanced Photon Source
MBP	maltose binding protein
MG	malachite green
μRA	microretarder array
NA	numerical aperture
NLO	nonlinear optical/nonlinear optics
NMF	non-negative matrix factorization
PD	photodiode
PEG	poly(ethylene glycol)
PMT	photomultiplier tube
R6G	rhodamine 6G
SHG	second harmonic generation

SONICC	second-order nonlinear imaging of chiral crystals
TC	tetracysteine
TPEF	two-photon excited fluorescence
TPE-UVF	two-photon excited UV fluorescence
UV	ultraviolet
UVF	UV fluorescence
XFEL	X-ray free-electron laser
XRD	X-ray diffraction

## ABSTRACT

Understanding the function and structure of a protein is crucial for informing on rational drug design and for developing successful drug candidates. However, this understanding is often limited by the protein pipeline, i.e. the necessary steps to go from developing protein constructs to generating high-resolution structures of macromolecules. Because each step of the protein pipeline requires successful completion of the prior step, bottlenecks are often created and therefore this process can take up to several years to complete. Addressing current limitations in the protein pipeline can help to reduce the time required to successfully solve the structure of a protein.

The field of nonlinear optical (NLO) microscopy provides a potential solution to many issues surrounding the detection and characterization of protein crystals. Techniques such as second harmonic generation (SHG) and two-photon excited UV fluorescence (TPE-UVF) have already been shown to be effective methods for the detection of proteins with high selectivity and sensitivity. Efforts to improve high throughput capabilities of SHG microscopy for crystallization trials resulted in development of a custom microretarder array ( $\mu$ RA) for depth of field (DoF) extension, therefore eliminating the need for z-scanning and reducing the overall data acquisition time. Further work was done with a commercially available  $\mu$ RA to allow for polarization dependent TPE-UVF. By placing the  $\mu$ RA in the rear conjugate plane of the beam path, the patterned polarization was mapped onto the field of view and polarization information was extracted from images by Fourier analysis to aid in discrimination between crystalline and aggregate protein.

Additionally, improvements to X-ray diffraction (XRD), the current gold standard for macromolecular structure elucidation, can result in improved resolution for structure determination. X-ray induced damage to protein crystals is one of the greatest sources of loss in resolution. Previous work has been done to implement a multimodal nonlinear optical (NLO) microscope into the beamline at Argonne National Lab. This instrument aids in crystal positioning for XRD experiments by eliminating the need for X-ray rastering and reduces the overall X-ray dosage to the sample. Modifications to the system to continuously improve the capabilities of the instrument were done, focusing on redesign of the beam path to allow for epi detection of TPE-UVF and building a custom objective for improved throughput of 1064 nm light. Furthermore, a computational method using non-negative matrix factorization (NMF) was employed for isolation



of unperturbed diffraction peaks and provided insight into the mechanism by which X-ray damage occurs. This work has the potential to improve the resolution of diffraction data and can be applied to other techniques where X-ray damage is of concern, such as electron microscopy.

## CHAPTER 1. INTRODUCTION

### 1.1 The role of the protein pipeline in rational drug design

The development of new drug candidates is an arduous process, often taking years before the drug makes it to market and can be used to treat patients.<sup>1</sup> For this reason, the ability to identify potential drug candidates with the highest chance of success is crucial and relies heavily on understanding the function of proteins. Because many diseases are caused by mutations to amino acids in proteins, successful drug candidates often target the mutations responsible for the disease. As such, having a clear understanding of a protein's structure and how the protein functions natively is beneficial to developing successful drug candidates. For a drug candidate to be effective, it should specifically target only the desired protein and location. Solving the structure of a protein informs on how that protein functions and provides more insight into how best to address the malfunctions caused by mutations to these proteins. This allows for drug candidates with the highest chance of success to be more readily identified.

X-ray diffraction (XRD) is commonly considered the “gold standard” for macromolecular structure determination. XRD was first used to solve the structure of a protein in 1958, when Max Perutz and John Kendrew used this technique to solve the structure of myoglobin, earning them the Nobel Prize in 1962.<sup>2</sup> Since then, XRD has been responsible for over 120,000 protein structure entries on the Protein Data Bank (PDB), more than all other structure determination techniques combined.<sup>3</sup> The ability to produce high quality protein crystals is crucial to generating high resolution structures that can inform on rational drug design. However, the path to producing these crystals involves many steps, each of which can be time consuming and difficult to optimize. Improvements in these steps would greatly decrease the amount of time needed to understand a protein and therefore would directly impact the drug discovery process.

Solving the structure of a protein involves multiple steps, many of which are time consuming and nontrivial to perform. There are five steps to the protein pipeline: 1) protein expression, 2) biochemical characterization, 3) crystallization, 4) optimization, and 5) structure determination (Figure 1.1). New protein targets are first cloned by insertion of modified DNA vectors into the appropriate cell line in order to produce the desired protein of interest. After expression, proteins are extracted from the cells and purified to remove cellular debris and

unwanted proteins. Purified proteins are then used to produce protein crystals, often requiring hundreds to thousands of different conditions with varying temperatures, pHs, buffers, and concentrations to fully optimize the crystallization protocol and achieve high quality crystals needed for X-ray crystallography experiments.<sup>4</sup> Each step of the protein pipeline relies on success of the previous step before moving forward in the process, often creating bottlenecks to solving the structure of a protein. Additionally, each step becomes increasingly more time consuming to perform. From start to finish, it can take up to several years to determine the structure of a protein. Improvements to any step in the protein pipeline can reduce the time and effort required to generate a protein structure.

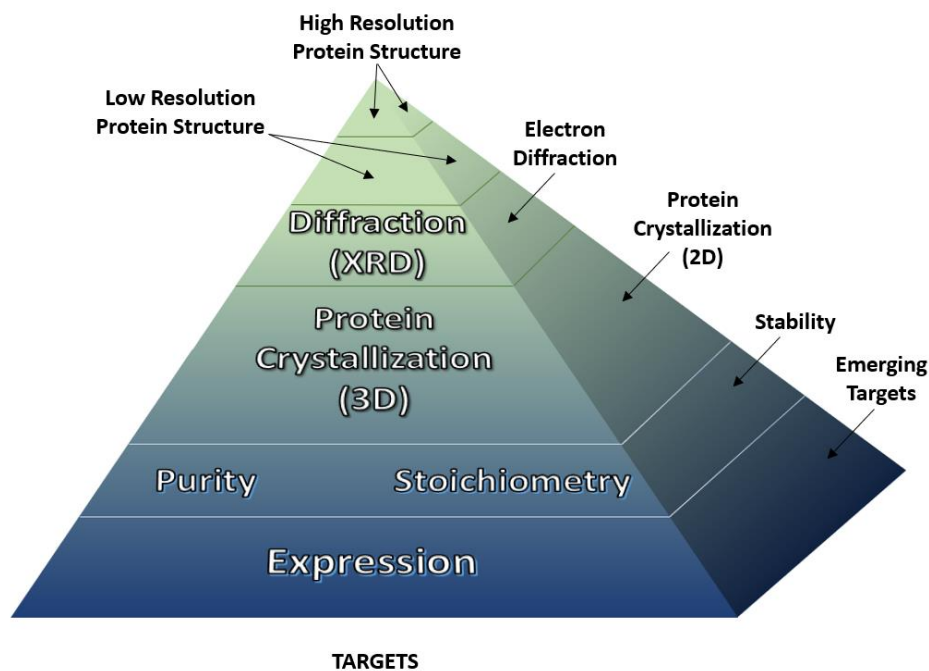


Figure 1.1 Protein structure determination pipeline.

## 1.2 Challenges and advances in protein detection and characterization

The process of optimizing protein crystals often uses a trial-and-error approach, requiring many crystallization trials to identify successful approaches for obtaining crystals. For this reason, there is a need for high-throughput crystal screening methods that allow for rapid detection of the presence of crystals in crystallization trials. Many different imaging approaches have been shown to be effective at detecting protein crystals. Some approaches such as bright field and ultraviolet

fluorescence imaging can be used to detect larger protein crystals, but also have a high rate of false negatives and therefore positive crystal hits often go undetected.<sup>5</sup> Other techniques that rely on the intrinsic fluorescence of proteins have recently been used for protein crystal detection, but are limited to proteins containing aromatic residues, such as tryptophan.<sup>6</sup> In the case of proteins that do not possess intrinsic fluorescence, UV light-based imaging modalities have been implemented for detection. However, exposure of UV light to proteins results in damage to disulfide bonds in the protein.<sup>7</sup> Additionally, proteins with no intrinsic fluorescence can be modified with covalently bound fluorophores, allowing them to be detected using fluorescence imaging techniques. Unfortunately, covalent modification has been shown to have adverse effects on protein folding, charge, and intermolecular contacts and therefore can complicate the crystallization process.<sup>8</sup> While extensive work has been done to develop novel techniques for high-throughput crystal screening, there is still room for improvement.

Understanding the functionality of a protein is aided by the ability to produce high resolution structures. However, the achievable resolution of a structure from XRD experiments is often limited due to X-ray induced damage to the crystal.<sup>9</sup> As crystals are exposed to X-ray radiation, the quality of the crystal begins to degrade and therefore so does the achievable resolution. Significant work has been done to address this issue. Some crystal positioning techniques that do not require X-ray rastering, and therefore less X-ray dose to the crystal, have been employed to achieve higher resolution in structure solutions.<sup>10</sup> X-ray free-electron lasers (XFELs) utilize a “diffract-before-destroy” approach and rely on serial crystallography to improve the quality of diffraction data.<sup>11</sup> Computational methods for recovering unperturbed structures have also shown promise for improving structure resolution in XRD experiments.<sup>12</sup> Ultimately, as protein crystals trend to increasingly smaller sizes and it becomes more difficult to solve the structure of these proteins, current structure determination techniques will continually be challenged in their ability to produce high-resolution structures.

### 1.3 Nonlinear optical imaging techniques

Second harmonic generation (SHG) microscopy has been demonstrated as an effective method for the detection and discrimination of protein crystals with the benefit of high sensitivity and selectivity.<sup>13</sup> In SHG, or the frequency doubling of light, two photons of a frequency  $\omega$  are converted to one photon at twice the frequency  $2\omega$  and half the wavelength, as shown in Figure

1.2. When a sample is excited by light, an SHG signal will be produced for crystalline materials that are non-centrosymmetric, meaning media with inversion symmetry are forbidden from generating SHG.<sup>14</sup> For this reason, SHG produces a signal with little to no background contribution from non-crystalline materials, such as aggregate and soluble protein, and therefore is highly advantageous in identifying between crystalline and aggregate protein. However, one limitation to SHG as an imaging technique for protein crystal detection lies within its symmetry requirements. Not all proteins will possess the necessary symmetry requirements to produce a detectable signal, limiting the applicability of this technique. Complementary NLO techniques can provide further insight into protein samples that are not detectable by SHG.

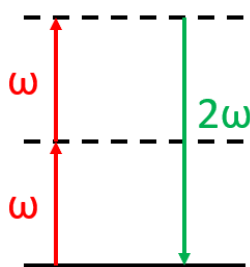


Figure 1.2 Energy diagram for second harmonic generation.

Two-photon UV fluorescence (TPE-UVF) utilizes the intrinsic fluorescence of proteins containing the amino acid tryptophan for detection.<sup>15</sup> In TPE-UVF, two photons of 532 nm light are combined to excite the 266 one-photon absorption band through vibrational relaxation, as shown in Figure 1.3. Additionally, this technique does not require use of a UV light source and therefore eliminates potential sample damage from UV light. TPE-UVF has been effectively used for detecting proteins, but cannot discriminate between aggregate and crystalline protein, as both forms will produce a fluorescence signal. Polarization measurements can be implemented in TPE-UVF to address this limitation, where crystalline protein will produce a different response compared to aggregate protein depending on the polarization state of light delivered to the sample.

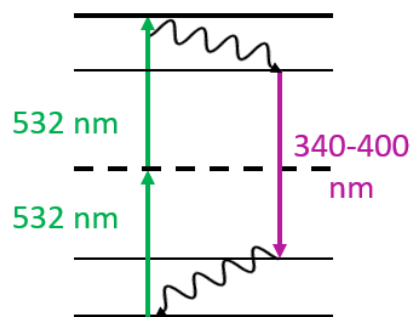


Figure 1.3 Energy diagram for two-photon excited UV fluorescence.

Nonlinear optical imaging techniques have shown promise for the detection of protein crystals with high sensitivity and selectivity. While techniques such as fluorescence microscopy can detect proteins containing a fluorescent amino acid, most commonly tryptophan, they are unable to discriminate between crystalline and aggregate protein. Combining both SHG and TPE-UVF techniques can provide a more complete picture of the sample and has been demonstrated as an effective modality for imaging protein crystals, as shown in Figure 1.4.<sup>15</sup>

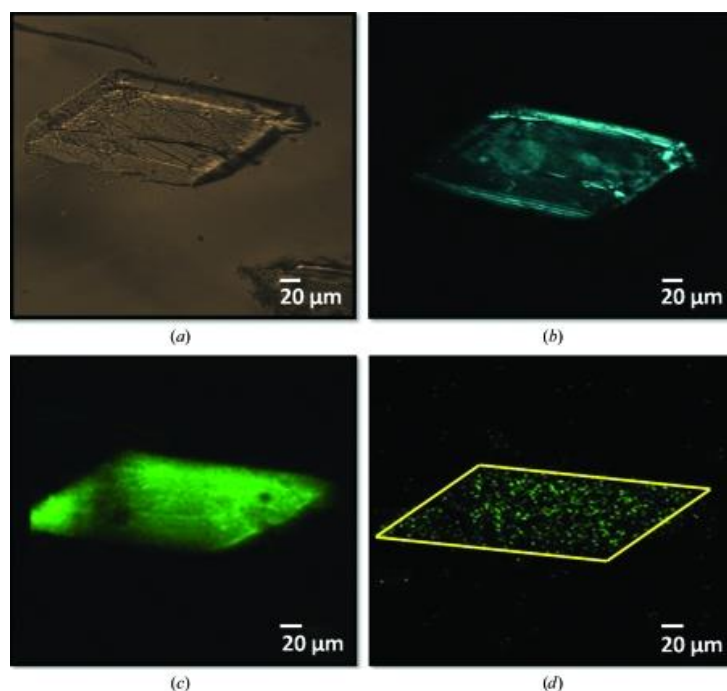


Figure 1.4 Multimodal crystal detection of an ABC maltose transporter protein; (a) bright field, (b) SHG, (c) and (d) TPE-UVF at 3 min and 3 sec acquisition time, respectively. Figure adapted from Madden et al, 2011.<sup>15</sup>

## 1.4 Dissertation overview

This dissertation will focus on novel techniques for addressing difficulties in the detection, characterization, and structure determination of macromolecules to improve on rational drug design.

Chapter 2 details a new computational method for isolating unperturbed diffraction peaks after X-ray diffraction data collection to address the issue of X-ray induced damage to protein crystals using a computational method, non-negative matrix factorization (NMF). In this work, NMF was applied to X-ray diffraction data at both cryogenic and room temperatures. NMF revealed the presence of three components, A, B, and C, that produce unique diffraction patterns. Further analysis of the decomposed data using kinetic modeling showed that the transition of these three components is sequential rather than stochastic, meaning component A transitions to component B and not component C. This finding provides insight into the mechanism by which X-ray damage occurs. Comparison of data collected at cryogenic and room temperature suggests that the mechanism of damage may differ at different temperatures. This work can potentially be applied to other techniques where radiation damage to crystals poses an issue, such as electron microscopy.

Chapter 3 provides a summary of work done in collaboration with Argonne National Laboratory to incorporate a multimodal nonlinear optical microscope into the X-ray beamline to aid in crystal positioning prior to X-ray diffraction. Previous work has been done to implement a multimodal NLO microscope that uses SHG and TPE-UVF to allow users to position the sample prior to XRD.<sup>16</sup> The standard method for crystal positioning involves raster scanning the sample to find areas of interest. This approach is time consuming and exacerbates the issue of X-ray damage, as the crystal is already perturbed by X-rays before any data collection occurs. By installing an NLO microscope into the beamline, SHG and TPE-UVF can be used to find the crystal without adding to the X-ray dosage and significantly reduce the time needed for crystal positioning. Modifications have since been made to the original beam path design to allow for efficient detection of TPE-UVF in an effort to suppress the backscattering of 532 nm light that overwhelms the PMT and prevents UV detection. Additionally, work has been done to develop a custom objective that has been optimized for the throughput of 1064 nm light. Future work will focus on developing a complementary objective that is optimized for the detection of UV light.

Chapter 4 focuses on using a custom designed microretarder array ( $\mu$ RA) for extending the depth of field for imaging. This optic consists of a repeating concentric design that results in polarization wavefront shaping capable of extending the depth of field (DoF). By extending the DoF in SHG imaging, the total data acquisition time was decreased by a factor of 3 compared to conventional z-scanning approaches. Furthermore, studies to assess the capability of this approach for high throughput crystal screening showed that more crystals were detected using the  $\mu$ RA than with the z-scanning approach. Experiments were conducted on a variety of different samples to demonstrate the wide range of applications this approach could potentially benefit.

In Chapter 5, a new approach for performing polarization dependent TPE-UVF imaging of protein crystals is described. This method utilizes a commercially available  $\mu$ RA that, when placed in the rear conjugate plane of the beam path, can be used to vary the polarization state across the field of view. This approach is advantageous in that the optic is easily retrofitted into existing beam paths and allows for rapid modulation of the polarization state of light. In addition, polarization dependent imaging using TPE-UVF provides the ability to discriminate between aggregate and crystalline protein. A computational approach to isolate the contributions from the responses of linearly and circularly polarized light through Fourier analysis was developed. Calculating the ratio between the linear and circular contributions provides insight into the nature of the sample.

In Chapter 6, preliminary results for conducting fluorescence recovery after photobleaching (FRAP) experiments at an X-ray beamline are discussed. In these experiments, lysozyme crystals were labeled with rhodamine 6G, both covalently bound and intercalated into the crystal lattice. Both samples were bleached using 532 nm light and then imaged using 1064 nm light to monitor the SHG signal recovery as temperature was increased. The experiments revealed a recovery of SHG intensity as the temperature of the cryogenic stream was increased from 100 K to 240 K, with the most recovery seen at 200 K. This finding is significant due to the known transition state of water at 200 K.<sup>17</sup> This transition corresponds to the point below which  $\alpha$  and  $\beta$  relaxation processes in glassy proteins merge, where  $\alpha$  represents the primary relaxation process and  $\beta$  represents polymer backbone motion.<sup>18</sup> Furthermore, it was observed that the samples with intercalated R6G required significantly more exposure for bleaching to be observed, suggesting that the dye molecules can more easily move in the crystal lattice since they are not bound to the crystal itself.



Chapter 7 details an effort to improve the number of proteins that can be probed using SHG by engineering a tetracysteine (TC) tag into a chaperone protein, maltose binding protein (MBP). The TC tag consists of the addition of four cysteines that can covalently bind to a FLaSH dye. Upon dye binding, a fluorescence signal can be detected. The motivation behind this approach was to “break” the centrosymmetry of SHG forbidden proteins through addition of the FLaSH dye, which is similar in structure to SHG active dyes such as rhodamine 6G (R6G) and malachite green (MG). In addition, by targeting a chaperone protein, the TC-MBP chaperone has the potential to improve purification and crystallization of proteins and could be expanded into aiding in packaging of monoclonal antibodies (mAb). Regrettably, while the TC tag was successfully engineered into MBP, crystal trials showed that the addition of the TC tag appeared to have negative effects in the ability to crystallize the protein. High quality crystals that could be analyzed via SHG were unable to be produced.

## 1.5 References

1. DiMasi, J.A. The value of improving the productivity of the drug development process. *Pharm. Econ.* **2002**, 20, 1-10.
2. De Chadarevian, S. John Kendrew and myoglobin: Protein structure determination in the 1950s. *Protein Sci.* **2018**, 27(6), 1136-1143.
3. Minor, W.; Dauter, Z.; Jaskolski, M. The young person’s guide to the PDB. *Postepy Biochem.* **2017**, 62(3), 242-249.
4. Krauss, I.R.; Merlino, A.; Vergara, A.; Sica, F. An overview of biological macromolecular crystallization. *Int. J. Mol. Sci.* **2013**, 14, 11643-11691.
5. Desbois, S.; Seabrook, S.A.; Newman, J. Some practical guidelines for UV imaging in the protein crystallization laboratory. *Acta Crystallogr. Sect. F Struct. Biol. Cryst. Commun.* **2013**, 69(2).
6. Ladokhin, A.S.; Jayasinghe, S.; White, S.H. How to measure and analyze tryptophan fluorescence in membranes properly, and why bother. *Anal. Biochem.* **2000**, 285(2), 235-245.
7. Vernede, X.; Lavault, B.; Ohana, J.; Nurizzo, D.; Joly, J.; Jacquamet, L.; Felisaz, F.; Cipriani, F.; Bourgeois, D. UV laser-excited fluorescence as a tool for the visualization of protein crystals mounted in loops. *Acta. Cryst.* **2006**, 62(3), 253-261.

8. McPherson, S.; Nguyen, C.; Cudney, R.; Larson, S.B. The role of small molecule additives and chemical modification in protein crystallization. *Cryst. Growth Des.* **2011**, *11*, 1469-1474.
9. Atakisi, H.; Conger, L.; Moreau, D.W.; Thorne, R.E. Resolution and dose dependence of radiation damage in biomolecular systems. *IUCrJ* **2019**, *6*(6), 1040-1053.
10. Madden, J.T.; Toth, S.J.; Dettmar, C.M.; Newman, J.A.; Oglesbee, R.A.; Hedderich, H.G.; Everly, R.M.; Becker, M.; Ronau, J.A.; Buchanan, S.K.; Cherezov, V.; Morrow, M.E.; Xu, S.; Ferguson, D.; Makarov, O.; Das, C.; Fischetti, B.; Simpson, G.J. Integrated nonlinear optical imaging microscope for on-axis crystal detection and centering at a synchrotron beam. *J. Synchrotron Rad.* **2013**, *20*, 531-540.
11. Liu, H.; Lee, W. The XFEL protein crystallography: developments and perspectives. *Int. J. Mol. Sci.* **2019**, *20*(14), 3421.
12. Borek, D.; Cymborowski, M.; Machius, M.; Minor, W.; Otwinowski, Z. Diffraction data analysis in the presence of radiation damage. *Acta Crystallogr. D Biol. Crystallogr.* **2010**, *66*(2), 426-436.
13. Wampler, R.D.; Kissick, D.J.; Dehen, C.J.; Gualtieri, E.J.; Grey, J.L.; Wang, H.; Thompson, D.H.; Cheng, J.; Simpson, G.J. Selective detection of protein crystals by second harmonic microscopy. *J. Am. Chem. Soc.* **2008**, *130*(43), 14076-14077.
14. Trzeciecki, M.; Dahn, A.; Hubner, W. Symmetry analysis of second-harmonic generation at surfaces of antiferromagnets. *Phys. Rev. B.* **1999**, *60*(2), 1144-1160.
15. Madden, J.T.; DeWalt, E.L.; Simpson, G.J. Two-photon excited UV fluorescence for protein crystal detection. *Acta Crystallogr. D Biol. Crystallogr.* **2011**, *67*(10), 839-846.
16. Madden, J.T.; Toth, S.J.; Dettmar, C.M.; Newman, J.A.; Oglesbee, R.A.; Hedderich, H.G.; Everly, R.M.; Becker, M.; Ronau, J.A.; Buchanan, S.K.; Cherezov, V.; Morrow, M.E.; Xu, S.; Ferguson, D.; Makarov, O.; Das, C.; Fischetti, R.; Simpson, G.J. Integrated nonlinear optical imaging microscope for on-axis crystal detection and centering at a synchrotron beamline. *J. Synch. Rad.* **2013**, *20*, 531-540.
17. Giovambattista, N.; Loerting, T.; Lukanov, B.; Starr, F.W. Interplay of the glass transition and liquid-liquid phase transition in water. *Sci. Rep.* **2012**, *390*(2), 1-8.
18. Smith, G.D.; Bedrov, D. Relationship between the  $\alpha$  and  $\beta$  relaxation processes in amorphous polymer: Insight from atomistic molecular dynamics simulations of 1,4-polybutadiene melts and blends. *J. Polym. Sci. B Polym. Phys.* **2007**, *45*, 627-643.

## **CHAPTER 2. NON-NEGATIVE MATRIX FACTORIZATION FOR ISOLATING DAMAGE-FREE REFLECTIONS IN MACROMOLECULAR SYNCHROTRON DATA COLLECTION**

### **2.1 Introduction**

Generation of high resolution structures of macromolecules enable rational drug design and provide direct insights into fundamental mechanisms of action in proteins and protein assemblies.<sup>1</sup> Currently, X-ray diffraction (XRD) serves as the most widely used approach for the generation of high-resolution structures supporting such efforts.<sup>2</sup> Advances in brightness of synchrotron facilities and improvements in detector speed/sensitivity are enabling XRD analysis on ever-smaller protein crystals.<sup>3</sup> However, damage induced by X-ray radiation ultimately limits the achievable resolution, by altering the sample during the measurement. These effects are exacerbated by advances in ever brighter X-ray sources enabling analysis of ever smaller crystals.<sup>4</sup>

An X-ray photon can interact with a crystalline sample in three ways: 1) elastic scattering, 2) inelastic scattering, and 3) the photoelectric effect, which generates high energy photoelectrons.<sup>5-8</sup> Each photoelectron produced by an X-ray photon can produce up to 500 secondary electrons at lower energy.<sup>9</sup> These secondary electrons have been implicated for the reductive processes that contribute to damage in the crystal and loss in XRD intensity.<sup>10</sup>

A substantial body of work has been directed toward mitigating radiation damage induced in protein crystals during XRD. Performing experiments under cryogenic conditions can significantly decrease the rate of induced radiation damage.<sup>11</sup> However, cryo-cooling of the crystals can lead to an increase in mosaicity, which results in a reduction in XRD signal to noise and an increase in spot overlap. Beam shaping to produce a “top-hat” beam profile has been used to reduce the non-uniform X-ray exposure associated with traditional Gaussian beam profiles.<sup>12</sup> While this method is a successful strategy, access is not broadly available. In addition, although the distribution of the X-ray exposure is altered under this approach, the total X-ray dosage is not reduced. There is evidence that free radicals generated during XRD can be removed using radical scavengers in an effort to reduce secondary radiation damage.<sup>13</sup> However, additives can complicate the crystallization process and there is a large variability in the success of this method. X-ray free-electron lasers (XFEL) have been demonstrated as an alternative source for XRD by utilizing a

“diffract-before-destroy” approach.<sup>14-16</sup> This method is effective for serial crystallography, but access to XFELs is currently highly limited, complicating widespread adoption.

As crystal sizes are reduced, current approaches and methods will be increasingly challenged. For every diffracted protein contributing to structure determination, approximately 10 photons are absorbed by the sample under the X-ray wavelengths routinely used for structure determination.<sup>17</sup> As such, computational methods designed to identify and remove X-ray-induced artifacts in recovered scattering patterns nicely complement experimental methods such as cryo-protection and X-ray beam-shaping. Analysis of radiation-induced changes using matrix singular value decomposition has been used to model radiation-induced changes in XRD intensities.<sup>18</sup> Independent component analysis unexpectedly identified a radiation-damage state of single thaumatin crystal corresponding to reduced disulfide bridges that produced a higher contrast structure than the zero-dose extrapolated state.<sup>19</sup> Another computational method, named “0-dose”, performs a least-squares fit of a damage model to the diffraction data to recover “decay factors” which are used to compute corrected XRD intensities.<sup>20</sup> Singular value decomposition has been applied to time-resolved XRD data as a noise reduction method to determine phase information and kinetic mechanisms of X-ray damage.<sup>21</sup> Finally, computational analysis of radiation-induced changes has been used to optimize strategies for data collection, analysis and phasing in XRD experiments.<sup>22</sup>

Here we describe a computational method for numerically isolating unperturbed peaks and monitoring the progression of chemically specific damage introduced upon X-ray exposure using NMF. The NMF algorithm is described elsewhere<sup>23-25</sup> and is detailed in the experimental methods section. NMF enabled decomposition of dose-dependent scattering patterns into a series of components based on the physical requirements of non-negative intensities for the individual reflections and non-negative amplitudes of the components. This analysis provided additional insight into the mechanism of radiation damage and enabled isolation of the initial unperturbed XRD pattern.

## 2.2 Methods

### 2.2.1 Sample preparation

The crystallization protocol for tetragonal lysozyme was adapted from a method previously reported in Yaoi, M. *et al.*<sup>26</sup> and further detailed in previous publications from our research group.<sup>27</sup>

For cryogenic XRD experiments, crystals were prepared in 96-well plates and then looped and flash-frozen in liquid nitrogen. For room temperature XRD experiments, crystals were grown in capillaries, which were then sealed with epoxy prior to mounting for XRD.

## 2.2.2 XRD data collection

All XRD data were collected at the Advanced Photon Source at Argonne National Laboratory using GM/CA beamline 23-ID-B. XRD of lysozyme under cryogenic conditions was acquired with a 20  $\mu\text{m}$ -diameter X-ray beam, 20 $\times$ 20  $\mu\text{m}$  cell size, with 1 s exposure time and full unattenuated beam and a detector distance of 600 mm. This process was repeated for a total of 90 cycles. To assess the X-ray damage caused by radiation in the mother liquor adjacent to a crystal, room temperature XRD was performed with a cell and beam size of 20 $\times$ 20  $\mu\text{m}$ , and a detector distance of 200 mm. Radiation was delivered at one spot on the crystal for 10 ms. After a 1-minute interregnum, the process was repeated for 5 cycles. A grid area was then selected surrounding the crystal and radiated at each stop in the grid with 1 s exposure time. Radiation of the previously selected spot on the crystal was repeated for another 5 cycles of 10 ms exposure time. A flowchart detailing the room temperature XRD data acquisition can be found in Figure 2.1.

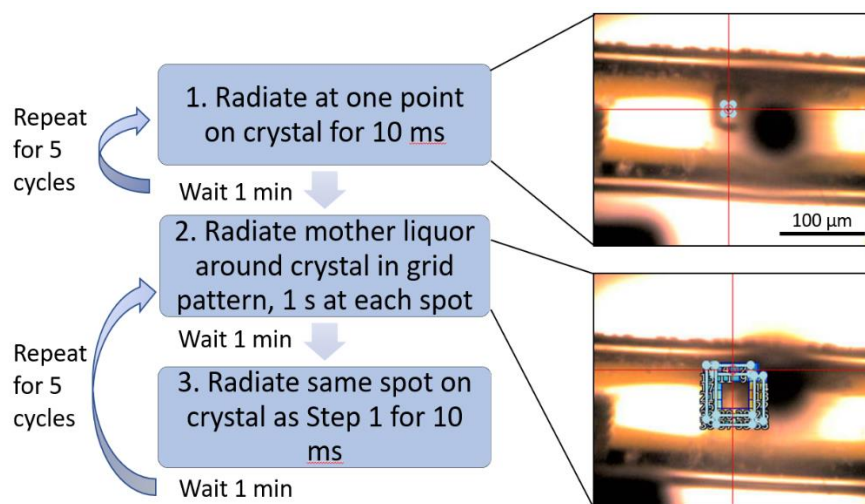


Figure 2.1 Schematic of the method used for data acquisition of room temperature XRD of lysozyme crystals, with images showing the area selected for radiation. Crystals were irradiated at one point for five, 10 ms periods initially, then the surrounding mother liquor was irradiated for 1 s followed by a 10 ms exposure at the original point on the crystal for five cycles.

### 2.2.3 Dimension reduction of XRD data

Peak-fitting was performed to identify discrete reflections arising from crystal diffraction. A MATLAB (MathWorks) script written in-house was used to read-in a series of synchrotron XRD patterns, which were all taken at the same location of the crystal repeatedly, i.e. with different accumulated X-ray dosage. The first step involved identification of peaks in the first image of the stack, and then tracking the intensities of these peaks through the stack of images. For image peak identification at a particular tilt angle, intensity-based threshold settings were applied on per pixel basis following background subtraction. Each individual peak was fit to a Gaussian, and the 99.95% confidence interval was used to track corresponding reflections throughout the data acquisition stack. Based on these criteria, the following information about individual peaks in each image was obtained, (i) index of peak in the image, (ii) number of pixels in the peak, (iii) X coordinate of the center of the peak, (iv) Y coordinate of the center of the peak, (v) integrated intensity of the peak, (vi) distance from the peak center to the center of the XRD image. The peak-identification results of the first XRD image served as a "library" or "reference" for subsequent XRD images. The program then compared the (X,Y) location and variance of peaks in a given image with corresponding parameters within the "library", which were scored as arising from the same reflection when overlapping within 99.95% confidence. Next, the integrated intensities of peaks scored to be from the same reflection within the image stack were arranged in a matrix D, with M rows and N columns, where M is the number of peaks in the peak library, and N is the total number of XRD images.

Note that MATLAB does not offer direct API for crystal file handling, specifically, crystal files in the format of Crystallographic Binary File (CBF).<sup>28</sup> CBF files consist of a ASCII header specifying the experimental parameters and the actual raw data set. To process just data matrix, we use GIXSGUI<sup>29</sup> to extract the data information in CBF files as purely numerical matrices for analyzing. After the matrices are decomposed, the numerical matrices are recombined with the original header to CBF format using the python module FabIO<sup>30</sup> so as to be solved in HKL2000 (HKL Research).

### 2.2.4 Non-negative matrix factorization (NMF)

NMF is a matrix decomposition method that uses an assumption of non-negativity to extract component spectra and concentrations from data sets. In NMF, a data matrix  $D$  is modeled as the linear combination of  $K$  components. These  $K$  components are described by their unique spectra,  $S$  and their concentrations,  $C$ . As shown in Equation 2.1, the data matrix  $D_{(M \times N)}$  is equal to the matrix multiplication of  $S_{(M \times K)}$  and  $C_{(K \times N)}$  where  $M$  is the number of spectral channels and  $N$  is the number of time or dose data points.

$$D_{(M \times N)} = S_{(M \times K)} C_{(K \times N)} \quad 2.1$$

If the value of  $K$  is unknown prior to analysis, an integer guess value is needed to perform NMF analysis. In practice, NMF analysis is commonly performed multiple times with different  $K$  values to determine the value of  $K$ .

NMF uses an iterative algorithm to recover the matrices  $S$  and  $C$  from matrix  $D$  in the following steps: i) An initial guess for  $S$  is used to solve for  $C$ , as shown in Equation 2.2.

$$C = (S^T S)^{-1} S^T D \quad 2.2$$

ii) The assumption of non-negativity is applied to matrix  $C$ . It is assumed that spectral and concentration values cannot be negative. Based on this assertion, all the negative elements of  $C$  are changed to zero. iii) This corrected matrix  $C$  is then used to solve for  $S$ , as shown in Equation 2.3.

$$S = D C^T (C C^T)^{-1} \quad 2.3$$

iii) The matrix  $S$  is also subjected to the same non-negativity constraint such that all negative elements of  $S$  are changed to zero. Steps i–iii are repeated until both matrices  $S$  and  $C$  converge to non-negativity (no negative elements).

### 2.2.5 Kinetic modeling

The change in concentration of the NMF components was modeled as a series of first-order kinetic processes using matrix methods.<sup>31</sup> A first-order reaction can be described by a system of differential equations.

$$\frac{d\overline{A}}{dt} = K\overline{A} \quad 2.4$$

where  $\frac{d\vec{A}}{dt}$  is a vector of length  $m$  of derivatives representing the change in concentration of a reactant or product with respect to time,  $K$  is a matrix of dimension  $m \times m$  of rate constants, and  $\vec{A}$  is a vector of length  $m$  of concentrations of reactants and products. As has been demonstrated previously,<sup>32</sup> this differential equation can be solved through diagonalization of  $K$  resulting in the following expression for the time-varying set of concentrations  $\vec{A}_t$ .

$$\vec{A}_t = (Pe^{\Lambda t}P^{-1})\vec{A}_0 \quad 2.5$$

where  $P$  is an orthonormal matrix of dimension  $m \times m$  and  $\Lambda$  is a diagonal matrix of dimension  $m \times m$  of eigenvalues for the matrix  $K$ , given by the following expression.

$$\Lambda = P^{-1}KP \quad 2.6$$

This relation is used in this work to generate the first-order fits to the change in component concentrations extracted via NMF. The matrix  $K$  was constrained to have 7 nonzero elements out of 16 total elements ( $m = 4$ ). The 7 nonzero elements corresponded to the following rate constants:  $k_{AB}$ ,  $k_{AC}$ ,  $k_{AD}$ ,  $k_{BC}$ ,  $k_{BD}$ , and  $k_{CD}$ . Only forward, irreversible reactions were considered in the kinetic analysis. Error in the rate constants was computed from the covariance matrix, which was calculated using Equation 2.7 with the covariance matrix  $C$  and the Jacobian of the fit  $J$ .

$$C = (J^T J)^{-1} \text{var}(\text{residuals}) \quad 2.7$$

## 2.3 Results and discussion

### 2.3.1 NMF decomposition of cryogenic lysozyme XRD

Changes in the dose-dependent XRD patterns at a single, fixed orientation and position for a lysozyme crystal under cryogenic conditions are presented in Figures 2.2 and 2.3. Integration of the collective set of diffracted peak intensities suggests only a relatively weak overall loss in total diffracted power with dose (see Fig. 2.3). However, decomposition by NMF reveals a significantly more interesting set of distinct transitions arising upon X-ray exposure. The decomposed scattering patterns, shown in Figure 2.2, exhibit differences in the location and number of high intensity peaks. Components B and C, which correspond to scattering patterns induced by X-ray exposure, have fewer high-intensity peaks than component A. The intensity of a reflection scales with the projected electron density along that  $(hkl)$  lattice plane. As such, it is somewhat surprising to observe such large relative differences within the scattering patterns for the decomposed structures. Most notably, it is interesting that the components B and C both still contain high-resolution



reflections, corresponding to high scattering angles. These features are inconsistent with models for damage based on global loss of overall order upon X-ray absorption.

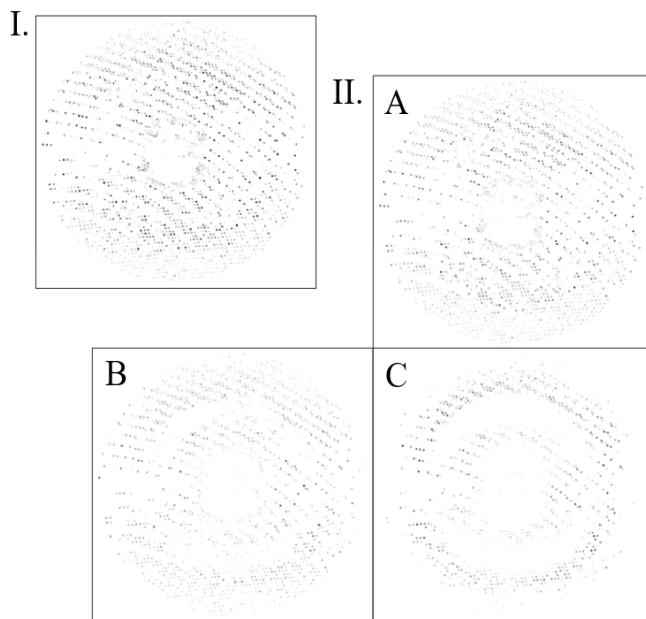


Figure 2.2 Decomposition of XRD peaks into NMF components. I) Initial XRD pattern of tetragonal lysozyme prior to decomposition. II) Components A-C generated from NMF decomposition of the original XRD pattern. Kinetic modeling revealed a sequential progression from  $A \rightarrow B \rightarrow C$  with increasing X-ray dose. These XRD patterns show a decrease in diffraction peak intensities in components B and C arising following X-ray exposure.

### 2.3.2 Kinetic analysis of NMF components

Analysis of the kinetics for dose-dependent evolution of the different components in Figure 2.3 is particularly intriguing. No kinetics constraints were imposed on the raw data when using NMF to select the different components. Nevertheless, the emerging sequential progression from  $A \rightarrow B \rightarrow C \rightarrow D$  (nondiffracting) that is clearly evident from cursory inspection of the dose-dependent behavior is striking. These trends strongly suggest a sequential series of structural changes induced upon X-ray absorption.

Classical matrix methods described in the Experimental Methods were used for first-order kinetic modeling to fit the variation in relative integrated intensities of the peaks to their respective components. The unperturbed protein had the highest overall integrated intensity following initial X-ray exposure, with small, but non-zero contributions present from components B and C.

Component A underwent rapid loss upon X-ray irradiation with a decay constant of  $0.0265 \pm 0.008$   $\text{MGy}^{-1}$ . While B experienced an initial rise and then fall, C showed a consistent increase and then maintained the same relative contributions even after going through high-energy radiation damage at the end of  $\sim 35$   $\text{MGy}$ .

The recovered rate constants give further insight into the mechanism of X-ray damage. The mathematical framework considered a set of possible forward reactions ( $A \rightarrow B$ ,  $A \rightarrow C$ ,  $A \rightarrow D$ ,  $B \rightarrow C$ ,  $B \rightarrow D$ , and  $C \rightarrow D$ ) and identified the reactions that matched the data. NMF component A only converted to component B, whereas component B converted to both components C and D (component D represents an amorphous component that is unable to diffract and is not shown in Fig. 2.3). Furthermore, the conversion from component A to B is rapid ( $k_{AB} = 0.265 \pm 0.008$ ) relative to the rate constants reporting the conversion of components B and C ( $k_{BC} = 0.050 \pm 0.006$ ,  $k_{BD} = 0.072 \pm 0.007$ ,  $k_{CD} = 0.013 \pm 0.003$ , all in units of  $\text{MGy}^{-1}$ , reported error is the standard deviation of the fit).

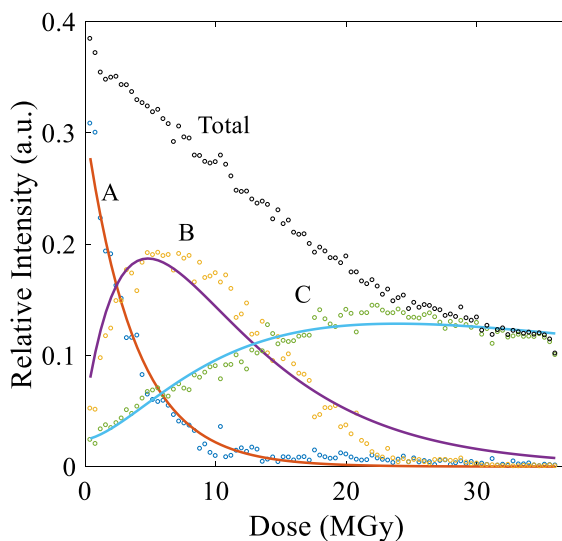


Figure 2.3 Kinetics of propagation of damage with X-ray dose in tetragonal lysozyme. Fitting to a kinetic model revealed a sequential progression from  $A \rightarrow B \rightarrow C$  with increasing X-ray dose. Recovered rate constants from the fit were:  $k_{AB} = 0.265 \pm 0.008$ ,  $k_{AC} = 0.000 \pm 0.008$ ,  $k_{AD} = 0.00 \pm 0.01$ ,  $k_{BC} = 0.050 \pm 0.006$ ,  $k_{BD} = 0.072 \pm 0.007$ , and  $k_{CD} = 0.013 \pm 0.003$ , all in units of  $\text{MGy}^{-1}$ . Reported error is the standard deviation of the fit.

### 2.3.3 NMF decomposition of room-temperature lysozyme XRD

Further studies were performed at room temperature to compliment measurements under cryogenic conditions. Crystal damage by free radicals arising from X-ray exposure around the crystal (i.e. in the mother liquor) was investigated. The results are outlined in Figure X.4, where (I) illustrates change in the overall integrated intensity of XRD peaks due to perturbations induced by radiation around the crystal at room temperature and (II) represents variation in the amplitudes of the three NMF components. The vertical lines on the x-axis signify the point at which the X-ray radiation was applied to the region surrounding the crystal. Initially, component A decreased and component B increased, as was also observed in the cryogenic studies shown in Figure X.3. As the crystal experienced significant perturbation induced by X-ray exposure to the region around the crystal, components A and B decreased to near baseline while component C increased to become the major contributor to the XRD pattern. The overall diffraction intensity in (I) was similar before and after X-ray exposure adjacent to the crystal, but the loss in amplitude of the component A and the dominance of a new species, component C, after X-ray exposure indicates significant dose-induced reorganization within the lattice. Without the application of NMF, the full effect of irradiating the region around the crystal would not have been observed from the change in overall integrated intensity alone.

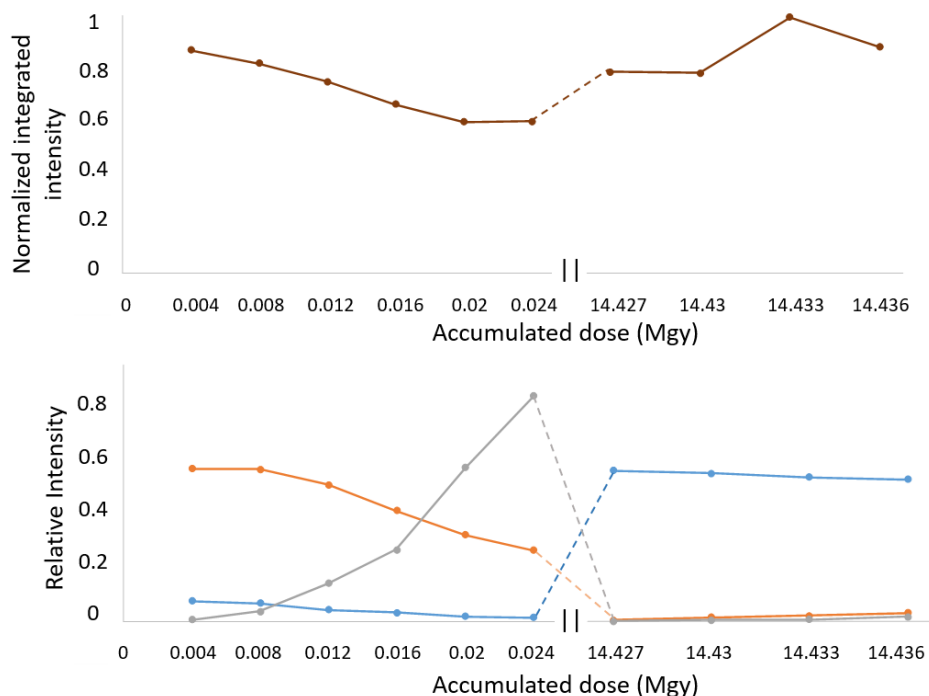


Figure 2.4 NMF analysis of indirect radiation damage to tetragonal lysozyme at room temperature. The vertical lines on the x-axis signify the point at which the X-ray radiation was applied to the region surrounding the crystal. I) The overall integrated intensity of the XRD peaks changes slightly due to damage induced by radiation around the crystal. II) NMF decomposition of the original XRD pattern into three components elucidates the significant change in composition as a function of radiation damage. Dashed lines are a visual aid and do not indicate continuity.

### 2.3.4 Discussion

One hypothesis for the observed behavior is transient, local heating from thermal accommodation of high-energy photoelectrons. The primary photoelectrons produced upon 1 Å X-ray absorption emerge with enough energy to exhibit a mean free path on the order of micrometers.<sup>33, 34</sup> Based on simulations, the primary photoelectron mean free path of <500 nm drives the overall spatial distribution of both primary and secondary photoelectrons under the cryogenic conditions most commonly used for structure determination.<sup>33, 34</sup> For the photon energies in these studies, the electron energy is deposited along a trajectory within a length scale of <500 nm. Since intermolecular energy transfer is slow relative to intramolecular transfer, we can assume that the energy dissipation along the primary electron path is constrained to a column with a cross-sectional area effectively similar to the size of a protein (e.g, 4 nm<sup>2</sup>). Dissipation of the entire energy bolus within that volume would therefore produce a temperature change of ~240

°C within the thermal vibrational relaxation time of a few tens of ps in a volume of  $\sim 2000 \text{ nm}^3$ . Even assuming the majority of that energy is sequestered in metastable structures suggests a localized temperature change sufficient to produce protein denaturation if maintained for any significant duration of time. Fortunately, heat is rapidly dissipated by thermal diffusion, with a thermal diffusivity of water of  $143 \text{ nm}^2/\text{ns}$  at room temperature.<sup>35</sup> Assuming comparable thermal diffusivity within cryogenically cooled vitreous ice, within 1 ns, thermal diffusion will spread the heat over a volume nearly 40-fold greater, corresponding to an increase in the temperature by only 6 °C. After 2 ns, the temperature change is reduced to  $\sim 3 \text{ °C}$ , approximately halving again each ns. This rapid but transitory intramolecular heating may potentially result in local bond-breaking events for proteins positioned close along the path of the initial photoelectron and dissipating large boluses of internal energy. These estimates of high but transient temperature changes contrast sharply from steady-state effects from X-ray absorption. Wallendar and Wallentin found through simulations that a nano-focused X-ray beam can produce a steady state temperature increase of only 8 °C within the region of X-ray irradiation.<sup>36</sup>

Under this transient local heating hypothesis, rapid heating would promote sequential breaking of the most chemically labile bonds in the protein structure, the result of which would produce a series of new protein species with different XRD patterns. Transient heating provides a possible mechanism for the significant molecular rearrangement required for substantive changes in the observed diffraction patterns, which would otherwise progress prohibitively slowly at cryogenic temperatures. However, the nature of the selectivity for specific reaction sites is not obvious through such a mechanism; in the limit of elevated temperatures, sufficient energy may be present to overcome numerous activation barriers, potentially reducing propensity for site-specific reactivity. This propensity toward reaction promiscuity may be tempered by kinetics, however. The highly transient (few ns) nature of the elevation in temperature would likely exclude any reactions requiring large-scale internal protein reorganization prior to reaction. Assuming the native protein contained several potential reaction sites accessible without substantial protein reorganization, it is not clear how rapid thermal activation alone could lead to a serial progression in chemical reactivity. In such a scenario, one would expect a branching ratio between all accessible reaction products, rather than a sequential reaction series.

Another hypothesis is that the crystal damage is caused by redox reactions initiated by the absorption of X-ray photons. Specific damage from molecular free radicals is possible at room

temperature by diffusion of small molecular radicals throughout the crystal, but under cryogenic conditions molecular diffusion no longer contributes to radical reactivity.<sup>37, 38</sup> Although molecular diffusion is insignificant at cryogenic temperatures, radical electrons can still demonstrate mobility through quantum tunneling along the protein backbone.<sup>13</sup> Unlike molecular diffusion, electron tunneling is temperature-independent and arises even at cryogenic temperatures.<sup>39, 40</sup> In the limit of fast electron redistribution throughout the protein, electron affinity dictates the probability of radical electron position. At low temperatures, even relatively subtle differences in electron affinity can result in significant preference for the lowest energy site by nature of the Boltzmann probability distribution. This principle explains the 'pecking order' of functional groups susceptible to specific structural damage. These reactive sites include disulfide bonds and carboxylate groups from aspartate and glutamate.<sup>41-44</sup> Evidence supporting the significance of radical reactions at cryogenic temperatures is also found from observations of reductions in X-ray induced damage upon incorporation of radical scavengers.<sup>45, 46</sup>

While tunneling provides an explanation for localization of radicals at specific intramolecular sites within a protein "primed" for reaction, the reaction itself to induce bond-breakage and/or major structural reorganization still has a prohibitively large activation barrier. It is unlikely that radical electron localization alone without reaction would be sufficient to induce the major changes in electron density observed in the X-ray scattering patterns associated with damage. Barriers of ~20 kcal/mol for S-S bond cleavage calculated by quantum chemistry are supported by mass spectrometric measurements of radical reactions.<sup>47</sup> At 100K, reaction rates with such barriers approach geologic timescales much slower than those calculated previously for molecular diffusion.

Consequently, we propose an explanation for the observed serial progression of changes in XRD in Figure X.3 through a stepwise pairing of these two effects: i) relatively rapid radical electron localization to sites with high electron affinity within the protein, priming those sites for reaction, and ii) local and highly transient heating from energy dissipation of hot photoelectrons to provide the energy to overcome barriers to reaction at those primed sites. This mechanism provides an explanation for the observation of serial reactivity through the priming of the sites of greatest electron affinity within each protein.

## 2.4 Conclusion

This two-step mechanism is supported by the use of NMF to recover the XRD patterns and relative abundances of three crystalline species that arose from radiation damage to a tetragonal lysozyme crystal. These collective results suggest promise for utilizing NMF for 1) the suppression of damage contributions in protein structure determination by integrating over the “damage-free” elements before solving the structure and 2) improving the fundamental understanding of the mechanism of sample damage in XRD. NMF could also potentially be used for other methods where radiation damage also impacts the measurement, such as electron microscopy.

## 2.5 References

1. Cheng, T. J.; Li, Q. L.; Zhou, Z. G.; Wang, Y. L.; Bryant, S. H., Structure-Based Virtual Screening for Drug Discovery: a Problem-Centric Review. *Aaps J.* **2012**, *14* (1), 133-141.
2. Garman, E. F., Developments in X-ray Crystallographic Structure Determination of Biological Macromolecules. *Science* **2014**, *343* (6175), 1102-1108.
3. Smith, J. L.; Fischetti, R. F.; Yamamoto, M., Micro-crystallography comes of age. *Curr. Opin. Struct. Biol.* **2012**, *22* (5), 602-612.
4. Lomb, L.; Barends, T. R. M.; Kassemeyer, S.; Aquila, A.; Epp, S. W.; Erk, B.; Foucar, L.; Hartmann, R.; Rudek, B.; Rolles, D.; Rudenko, A.; Shoeman, R. L.; Andreasson, J.; Bajt, S.; Barthelmeß, M.; Barty, A.; Bogan, M. J.; Bostedt, C.; Bozek, J. D.; Caleman, C.; Coffee, R.; Coppola, N.; DePonte, D. P.; Doak, R. B.; Ekeberg, T.; Fleckenstein, H.; Fromme, P.; Gebhardt, M.; Graafsma, H.; Gumprecht, L.; Hampton, C. Y.; Hartmann, A.; Hauser, G.; Hirsemann, H.; Holl, P.; Holton, J. M.; Hunter, M. S.; Kabsch, W.; Kimmel, N.; Kirian, R. A.; Liang, M. N.; Maia, F.; Meinhart, A.; Marchesini, S.; Martin, A. V.; Nass, K.; Reich, C.; Schulz, J.; Seibert, M. M.; Sierra, R.; Soltau, H.; Spence, J. C. H.; Steinbrener, J.; Stellato, F.; Stern, S.; Timneanu, N.; Wang, X. Y.; Weidenspointner, G.; Weierstall, U.; White, T. A.; Wunderer, C.; Chapman, H. N.; Ullrich, J.; Struder, L.; Schlichting, I., Radiation damage in protein serial femtosecond crystallography using an x-ray free-electron laser. *PhRvB* **2011**, *84* (21), 6.
5. Ravelli, R. B. G.; Garman, E. F., Radiation damage in macromolecular cryocrystallography. *Curr. Opin. Struct. Biol.* **2006**, *16* (5), 624-629.
6. Ankudinov, A. L.; Rehr, J. J., Theory of solid-state contributions to the x-ray elastic scattering amplitude. *PhRvB* **2000**, *62* (4), 2437-2445.
7. Ament, L. J. P.; van Veenendaal, M.; Devereaux, T. P.; Hill, J. P.; van den Brink, J., Resonant inelastic x-ray scattering studies of elementary excitations. *Rev. Mod. Phys.* **2011**, *83* (2), 63.

8. Dyson, N. A., *X-rays in Atomic and Nuclear Physics*. Cambridge University Press: 2005.
9. O'Neill, P.; Stevens, D. L.; Garman, E. F., Physical and chemical considerations of damage induced in protein crystals by synchrotron radiation: a radiation chemical perspective. *J. Synchrot. Radiat.* **2002**, *9*, 329-332.
10. Coleman, C.; Ortiz, C.; Marklund, E.; Bultmark, F.; Gabrysch, M.; Parak, F. G.; Hajdu, J.; Klintenberg, M.; Timneanu, N., Radiation damage in biological material: Electronic properties and electron impact ionization in urea. *Epl* **2009**, *85* (1), 6.
11. Garman, E., 'Cool' crystals: macromolecular cryocrystallography and radiation damage. *Curr. Opin. Struct. Biol.* **2003**, *13* (5), 545-551.
12. Laundry, D.; Alianelli, L.; Sutter, J.; Evans, G.; Sawhney, K., Surface profiling of X-ray mirrors for shaping focused beams. *Opt. Express* **2015**, *23* (2), 1576-1584.
13. Murray, J.; Garman, E., Investigation of possible free-radical scavengers and metrics for radiation damage in protein cryocrystallography. *J. Synchrot. Radiat.* **2002**, *9*, 347-354.
14. Patterson, B. D., Crystallography using an X-ray free-electron laser. *Crystallogr. Rev* **2014**, *20* (4), 242-294.
15. Amin, M.; Askerka, M.; Batista, V. S.; Brudvig, G. W.; Gunner, M. R., X-ray Free Electron Laser Radiation Damage through the S-State Cycle of the Oxygen-Evolving Complex of Photosystem II. *J. Phys. Chem. B* **2017**, *121* (40), 9382-9388.
16. Chernev, P.; Zaharieva, I.; Rossini, E.; Galstyan, A.; Dau, H.; Knapp, E. W., Merging Structural Information from X-ray Crystallography, Quantum Chemistry, and EXAFS Spectra: The Oxygen-Evolving Complex in PSII. *J. Phys. Chem. B* **2016**, *120* (42), 10899-10922.
17. Murray, J. W.; Rudino-Pinera, E.; Owen, R. L.; Grininger, M.; Ravelli, R. B. G.; Garman, E. F., Parameters affecting the X-ray dose absorbed by macromolecular crystals. *J. Synchrot. Radiat.* **2005**, *12*, 268-275.
18. Borek, D.; Dauter, Z.; Otwinowski, Z., Identification of patterns in diffraction intensities affected by radiation exposure. *J. Synchrot. Radiat.* **2013**, *20*, 37-48.
19. Borek, D.; Bromberg, R.; Hattne, J.; Otwinowski, Z., Real-space analysis of radiation-induced specific changes with independent component analysis. *J. Synchrot. Radiat.* **2018**, *25*, 451-467.
20. Diederichs, K.; McSweeney, S.; Ravelli, R. B. G., Zero-dose extrapolation as part of macromolecular synchrotron data reduction. *Acta Crystallogr. Sect. D-Biol. Crystallogr.* **2003**, *59*, 903-909.



21. Schmidt, M.; Rajagopal, S.; Ren, Z.; Moffat, K., Application of singular value decomposition to the analysis of time-resolved macromolecular X-ray data. *Biophys. J.* **2003**, *84* (3), 2112-2129.
22. Borek, D.; Cymborowski, M.; Machius, M.; Minor, W.; Otwinowski, Z., Diffraction data analysis in the presence of radiation damage. *Acta Crystallogr. Sect. D-Struct. Biol.* **2010**, *66*, 426-436.
23. Paatero, P.; Tapper, U., Positive matrix factorization - a nonnegative factor model with optimal utilization of error-estimates of data values. *Environmetrics* **1994**, *5* (2), 111-126.
24. Wang, W. W.; Cichocki, A.; Chambers, J. A., A Multiplicative Algorithm for Convolutional Non-Negative Matrix Factorization Based on Squared Euclidean Distance. *ITSP* **2009**, *57* (7), 2858-2864.
25. Griffin, S. R.; Biechele-Speziale, J. A.; Smith, C. J.; You-Dow, X.; White, J. K.; Zhang, S. W.; Novak, J.; Liu, Z.; Simpson, G. J., Iterative Non-Negative Matrix Factorization Filter for Blind Deconvolution in Photon/Ion Counting. *Anal. Chem.* **2019**, *91* (8), 5286-5294.
26. Yaoi, M.; Adachi, M.; Takano, K.; Matsumura, H.; Inoue, T.; Mori, Y.; Sasaki, T., Effect of stirring method on protein crystallization. *Japanese Journal of Applied Physics Part 2-Letters & Express Letters* **2004**, *43* (10A), L1318-L1319.
27. Newman, J. A.; Scarborough, N. M.; Pogranichniy, N. R.; Shrestha, R. K.; Closser, R. G.; Das, C.; Simpson, G. J., Intercalating dyes for enhanced contrast in second-harmonic generation imaging of protein crystals. *Acta Crystallogr. Sect. D-Struct. Biol.* **2015**, *71*, 1471-1477.
28. Bernstein, H.; Hammersley, A., Specification of the Crystallographic Binary File (CBF/imgCIF). *International Tables for Crystallography* **2006**.
29. Jiang, Z., GIXSGUI: a MATLAB toolbox for grazing-incidence X-ray scattering data visualization and reduction, and indexing of buried three-dimensional periodic nanostructured films. *Journal of Applied Crystallography* **2015**, *48*, 917-926.
30. Knudsen, E. B.; Sorensen, H. O.; Wright, J. P.; Goret, G.; Kieffer, J., FabIO: easy access to two-dimensional X-ray detector images in Python. *Journal of Applied Crystallography* **2013**, *46*, 537-539.
31. Steinfeld, J. I.; Francisco, J. S.; Hase, W. L., *Chemical kinetics and dynamics*. Prentice Hall Englewood Cliffs (New Jersey): 1989; Vol. 3.
32. Berberansantos, M. N.; Martinho, J. M. G., The integration of kinetic rate-equations by matrix-methods. *Journal of Chemical Education* **1990**, *67* (5), 375-379.

33. Sanishvili, R.; Yoder, D. W.; Pothineni, S. B.; Rosenbaum, G.; Xu, S. L.; Vogt, S.; Stepanova, S.; Makarov, O. A.; Corcoran, S.; Benn, R.; Nagarajan, V.; Smith, J. L.; Fischetti, R. F., Radiation damage in protein crystals is reduced with a micron-sized X-ray beam. *Proc. Natl. Acad. Sci. U. S. A.* **2011**, *108* (15), 6127-6132.
34. Nave, C.; Hill, M. A., Will reduced radiation damage occur with very small crystals? *J. Synchrot. Radiat.* **2005**, *12*, 299-303.
35. Blumm, J.; Lindemann, A., Characterization of the thermophysical properties of molten polymers and liquids using the flash technique. *High Temp. High Press* **2003**, *35* (36), 627.
36. Wallander, H.; Wallentin, J., Simulated sample heating from a nanofocused X-ray beam. *J. Synchrot. Radiat.* **2017**, *24*, 925-933.
37. Garman, E. F., Radiation damage in macromolecular crystallography: what is it and why should we care? *Acta Crystallogr. Sect. D-Biol. Crystallogr.* **2010**, *66*, 339-351.
38. Weik, M.; Colletier, J. P., Temperature-dependent macromolecular X-ray crystallography. *Acta Crystallogr. Sect. D-Biol. Crystallogr.* **2010**, *66*, 437-446.
39. Jones, G. D. D.; Lea, J. S.; Symons, M. C. R.; Taiwo, F. A., Structure and mobility of electron gain and loss centers in proteins. *Nature* **1987**, *330* (6150), 772-773.
40. Dick, L. A.; Malfant, I.; Kuila, D.; Nebolsky, S.; Nocek, J. M.; Hoffman, B. M.; Ratner, M. A., Cryogenic electron tunneling within mixed-metal hemoglobin hybrids: Protein glassing and electron-transfer energetics. *J. Am. Chem. Soc.* **1998**, *120* (44), 11401-11407.
41. Carpentier, P.; Royant, A.; Weik, M.; Bourgeois, D., Raman-Assisted Crystallography Suggests a Mechanism of X-Ray-Induced Disulfide Radical Formation and Reparation. *Structure* **2010**, *18* (11), 1410-1419.
42. Weik, M.; Ravelli, R. B. G.; Kryger, G.; McSweeney, S.; Raves, M. L.; Harel, M.; Gros, P.; Silman, I.; Kroon, J.; Sussman, J. L., Specific chemical and structural damage to proteins produced by synchrotron radiation. *Proc. Natl. Acad. Sci. U. S. A.* **2000**, *97* (2), 623-628.
43. Burmeister, W. P., Structural changes in a cryo-cooled protein crystal owing to radiation damage. *Acta Crystallogr. Sect. D-Struct. Biol.* **2000**, *56*, 328-341.
44. Ravelli, R. B. G.; McSweeney, S. M., The 'fingerprint' that X-rays can leave on structures. *Structure* **2000**, *8* (3), 315-328.
45. Lange, M.; Weiland, B.; Huttermann, J., Influence of electron scavengers on the radical formation in thymidine-5'-monophosphate and DNA in frozen aqueous-solution and glasses. *Int. J. Radiat Biol.* **1995**, *68* (4), 475-486.

46. Owen, R. L.; Axford, D.; Nettleship, J. E.; Owens, R. J.; Robinson, J. I.; Morgan, A. W.; Dore, A. S.; Lebon, G.; Tate, C. G.; Fry, E. E.; Ren, J. S.; Stuart, D. I.; Evans, G., Outrunning free radicals in room-temperature macromolecular crystallography. *Acta Crystallogr. Sect. D-Struct. Biol.* **2012**, *68*, 810-818.
47. Sohn, C. H.; Gao, J.; Thomas, D. A.; Kim, T.-Y.; Goddard Iii, W. A.; Beauchamp, J. L., Mechanisms and energetics of free radical initiated disulfide bond cleavage in model peptides and insulin by mass spectrometry. *Chemical science* **2015**, *6* (8), 4550-4560.

## CHAPTER 3. MODIFICATIONS TO A MULTIMODAL NONLINEAR OPTICAL MICROSCOPE INSTALLED AT A SYNCHROTRON

### 3.1 Introduction

X-ray diffraction is often considered the gold standard for structure determination of macromolecules. As improvements to X-ray sources have allowed for tighter beam focusing, structure determination of smaller crystals has become possible. However, this introduces new challenges associated with crystal positioning. In order to produce a high-resolution structure, proper positioning of the crystal prior to diffraction is crucial. While high-throughput methods for crystal positioning are ideal, these techniques struggle with smaller, more complex protein crystals. Currently, X-ray rastering is most commonly used for crystal positioning. In this approach, a focused X-ray beam is rastered across the area of interest.<sup>1</sup> The resulting diffraction data are used to identify locations with the strongest diffraction and position these areas of the crystal in the field of view.

Despite being an effective approach for crystal positioning, raster scanning does have limitations. Raster scanning can be relatively slow, taking several minutes to an hour per sample.<sup>2</sup> Usually, an initial raster scan is performed and then refined to a smaller area to produce the highest quality results. As the total number of pixels for the raster scan increases, so does the overall data acquisition time. Some advances have been made to reduce the time need for raster scanning, such as using single-photon-counting arrays to reduce integration times, but ultimately the data acquisition time is limited by the ability to achieve sufficient signal to noise.<sup>3</sup> Additionally, raster scanning introduces X-ray dose to the sample before data acquisition begins, exacerbating the issue of X-ray damage in protein crystals.<sup>4</sup>

Nonlinear optical imaging techniques have shown promise as alternative approaches for protein crystal detection.<sup>5</sup> Second harmonic generation (SHG) is a highly selective technique capable of detecting noncentrosymmetric crystalline material. Additionally, SHG is symmetry forbidden in disordered media, such as amorphous or soluble protein, and therefore can selectively detect protein crystals with a negligible background contribution.<sup>5</sup> For the percentage of protein crystals that are centrosymmetric and therefore do not produce a strong SHG signal, two-photon excited UV fluorescence (TPE-UVF) provides a complementary method. Any protein containing aromatic side-chains, most commonly tryptophan, will produce intrinsic fluorescence and are

detectable by TPE-UVF.<sup>6</sup> This technique has the added benefit of identifying between protein crystals and salt crystals, which can appear via SHG.<sup>7</sup> Use of NLO techniques for crystal positioning requires no additional X-ray dose to the sample and significantly decreases the data acquisition time, with images taking only a few seconds to obtain. Access to these techniques at synchrotron facilities could greatly improve crystal positioning and increased resolution in structures obtained through XRD.

Previous work has been done to implement a multimodal nonlinear optical microscope into the GM/CA 23-ID-B beamline at the Advanced Photon Source (APS) at Argonne National Lab.<sup>8</sup> The NLO microscope, shown in Figure 3.1, is the first to be installed at a synchrotron source and allows for SHG and TPE-UVF as tools for crystal detection prior to X-ray diffraction. Use of this microscope can inform on crystal positioning without raster scanning, decreasing the overall X-ray dosage induced to the sample. Additionally, access to these imaging modalities can have further benefits to XRD experiments and sample analysis. For example, access to this microscope lead to the development of a sparse supervised learning approach for dynamic sampling that also reduces the X-ray dosage and decreases data acquisition by using previous data acquired to inform upon the most information-rich location in the sample.<sup>9</sup>

To continue improving the capabilities of the NLO microscope and to make the instrument more applicable to general users, modifications were made to the existing microscope. A beam path redesign was completed to allow for epi detection of TPE-UVF and to optimize the system for this modality. Additionally, a custom objective was made to allow for higher throughput of IR light to improve the SHG capabilities of the microscope. Future work will focus on developing a similar objective optimized for transmission of 532 nm and UV light.

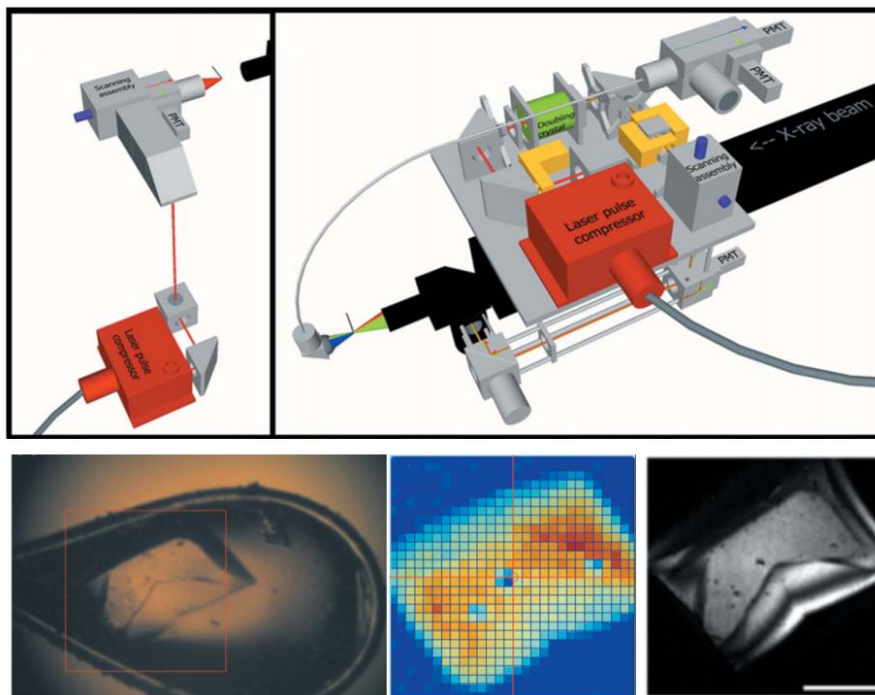


Figure 3.1 Schematic of the original beam path design of the nonlinear optical microscope installed at the beamline 23-ID-B at Argonne National Lab; BF, raster scan, and SHG images of lysozyme are shown to demonstrate how SHG can be used for crystal positioning. Adapted from Madden et al, 2013.

## 3.2 Methods

### 3.2.1 Beam path modifications

To optimize the microscope for TPE-UVF detection, a redesign of the beam path was completed. A schematic depicting the changes to the beam path is shown in Figure 3.2. A photomultiplier tube (PMT) sensitive to UV light was added into the beam path in the epi direction for detection of the TPE-UVF signal. Two long-pass dichroic mirrors (DCM) purchased from Edmund Optics, allowing for reflection of UV light and transmission of 532 nm and 1064 nm light were added to the beam path. The pre-existing fiber coupling the signal given off by samples to the detectors, shown in Figure 3.1, was removed and replaced with an SHG-sensitive PMT. Plano-convex lenses with a focal length of 25 mm were placed before both the SHG and TPE-UVF PMTs to focus the signal onto the face of the PMTs. All pre-existing detectors, boxed in red in Figure 3.1, were removed or repositioned.

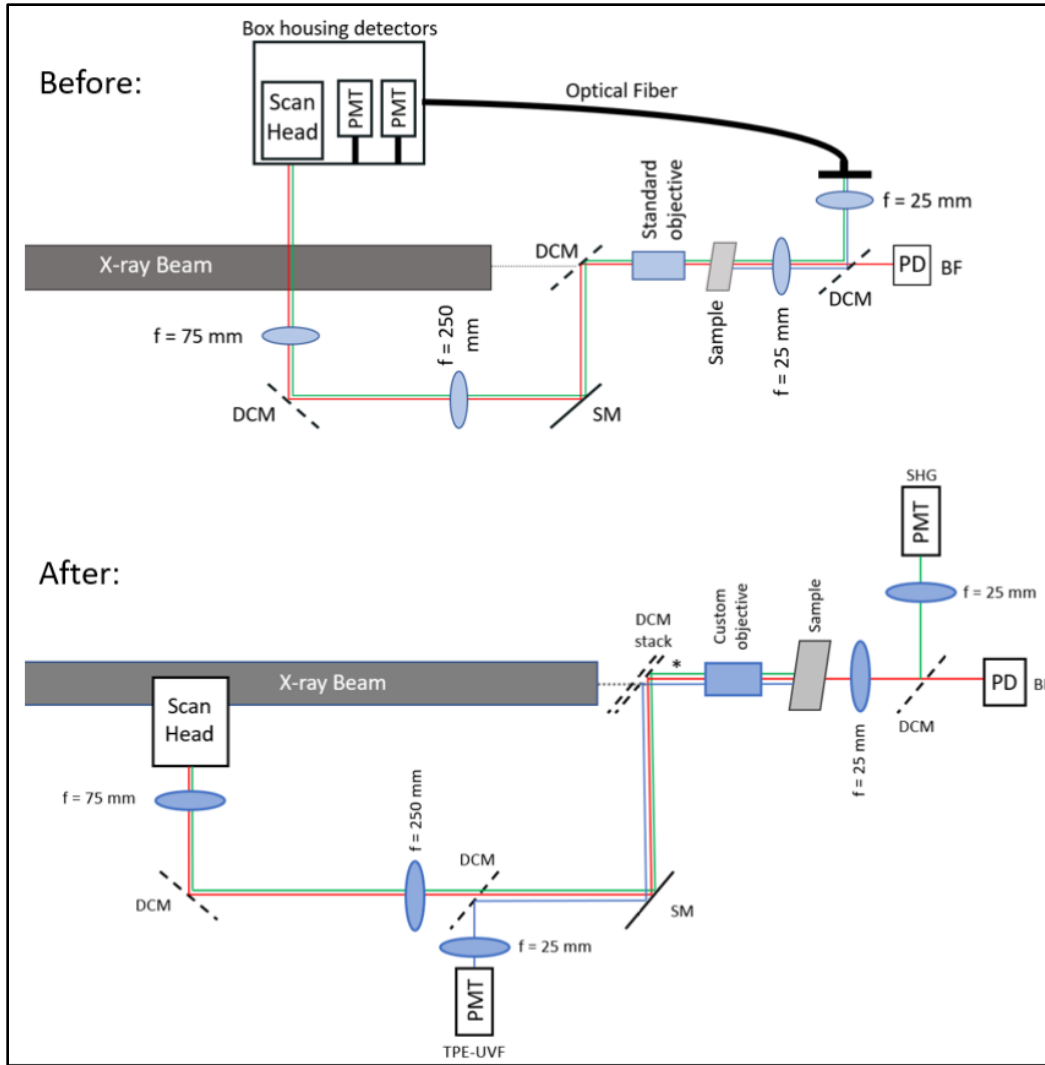


Figure 3.2 Schematic of the beam path before and after redesign. Note, scan head was not moved in the beam path, just for purposes of depicting the schematic.

### 3.2.2 Design of custom objective

A custom designed objective was built for improved throughput of 1064 nm light and therefore improved SHG detection. Commercially available objectives for this purpose exist but drilling a hole through the lenses of these objectives to accommodate the X-ray beam is non-trivial. Designing a custom objective with easier access to lenses to drill holes through provides an alternative solution. The custom objective consisted of eight lenses that were coated with a multilayer, antireflective thin film (V coating in Table 3.1) to allow for better transmission of 532 nm and 1064 nm light. Lens specifications are shown in Table 3.1. Four of these lenses are plano-convex, with focal lengths of 60 mm and 75 mm. The other four lenses are plano-concave, as

indicated by the negative focal length values. All lenses were purchased from Thorlabs. Holes were drilled through each lens by Jordan Smith in the glass blowing lab at Purdue University. All lenses were housed in a lens tube with SM1 threading, making the objective 68.6 mm in length with a radius of 30.5 mm. A schematic of the objective is shown in Figure 3.3.

Table 3.1 Specifications of lenses in the custom-built objective.

#Lens	L1	L2	L3	L4	L5	L6	L7	L8
Focal length	75 mm	-100 mm	75 mm	60 mm	75 mm	-100 mm	-100 mm	-75 mm
Coating	V	V	V	C	V	V	V	V

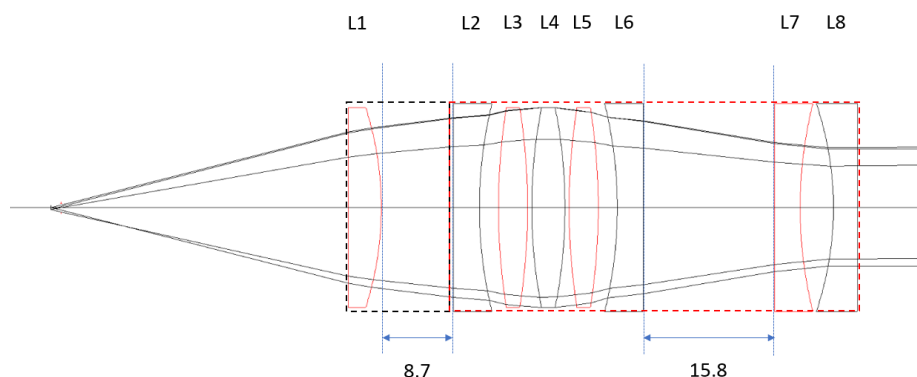


Figure 3.3 Schematic of custom-built objective, consisting of 8 lenses with varying focal lengths.

### 3.2.3 Data acquisition

All power readings were acquired using a wireless power meter with a thermal sensor from Thorlabs (PM160). Images were acquired with the custom objective and an Optem long-working distance objective (28-21-10) with a ~1.2 mm hole drilled through the optics to accommodate the X-ray beam. Bright field and SHG images were acquired using 1064 nm light set to the maximum power allowed.

## 3.3 Results and discussion

### 3.3.1 Discussion of modifications

Prior to modifications, the TPE-UVF modality of the NLO microscope was unable to successfully detect samples. The hypothesis for this issue was that the PMT was saturated with



residual 532 nm light from the fundamental laser beam and therefore was overpowering the UV signal. Efforts to suppress the 532 nm light were unsuccessful. Changing the beam path to allow for epi TPE-UVF detection provides a solution to this problem, as the 532 nm light becomes easier to suppress. To achieve this, a UV-sensitive PMT was placed in the beam path, after the scan head but before the sample plane, as shown in Figure 3.2. A bandpass filter was placed in front of the PMT to block any 532 nm light from interfering with the UV signal. In order to incorporate epi TPE-UVF into the system, a dichroic mirror reflecting UV light was added to the beam path to direct the UV signal back to the PMT. Unfortunately, a dichroic mirror with all the specifications needed to reflect UV, 532 nm, and 1064 nm light was not available, so multiple dichroic mirrors were sandwiched together with oil holding them together. Another dichroic mirror reflecting UV light and transmitting 532 and 1064 nm light was placed directly before the PMT to direct the UV light to the detector. This required addition of a cage cube with kinetic mount for adjustment of the filter. Additionally, to improve the quality of the SHG imaging modality, the fiber coupling the signal produced by the sample to the detectors was removed completely and replaced with a PMT sensitive to the SHG signal. With a shorter distance to travel, this setup should improve the amount of SHG signal making it to the detector. The redesign also simplifies alignment of the system, which previously has been nontrivial to do.

While SHG images with comparable signal to noise to the previous beam path design were obtained with the redesigned beam path, a TPE-UVF signal was not detected despite alignment of the system. The working hypothesis for this issue is that the custom-built objective, which is optimized for 1064 nm light throughput, has coatings that prevent transmission of the UV signal and therefore no signal is detected by the PMT.

### 3.3.2 Testing the custom objective

Extensive experiments were done to assess the performance of the custom-built objective. Power reading measurements were taken using both the custom objective and the standard Optem objective to compare the throughput of both objectives. The results of these experiments are shown in Table 3.2. With the custom objective, there was a 3x increase in power throughput for 1064 nm light compared to the standard Optem objective.

Table 3.2 Power readings measured at the sample plane with the custom-built objective and Optem objective installed in the system.

Objective	Beam scanning, 1064 nm	Non-scanning, 1064 nm
Custom-built objective	230 mW	240 mW
Optem with hole	63 mW	70 mW

Bright field and SHG images were acquired with both objectives using BaTiO<sub>3</sub> as a standard sample to ascertain the image quality of the custom objective compared to the standard objective. The images are shown in Figure 3.X. Using the same initial power input for all images, the bright field images for both objectives were comparable in quality. Note that the size of the field of views differ between the objectives, with the custom objective having a 1.5x lower magnification than the Optem objective and therefore a larger field of view. Comparing the two SHG images, a clear increase in SHG signal was seen with the custom objective. While with the Optem objective only some particles were faintly visible, the custom objective produced such bright SHG signal that the PMT was saturated due to the increased power throughput for 1064 nm light. It should be noted that TPE-UVF images were not able to be acquired with the objective, most likely due to the coatings of the lenses preventing epi detection of the UV signal.

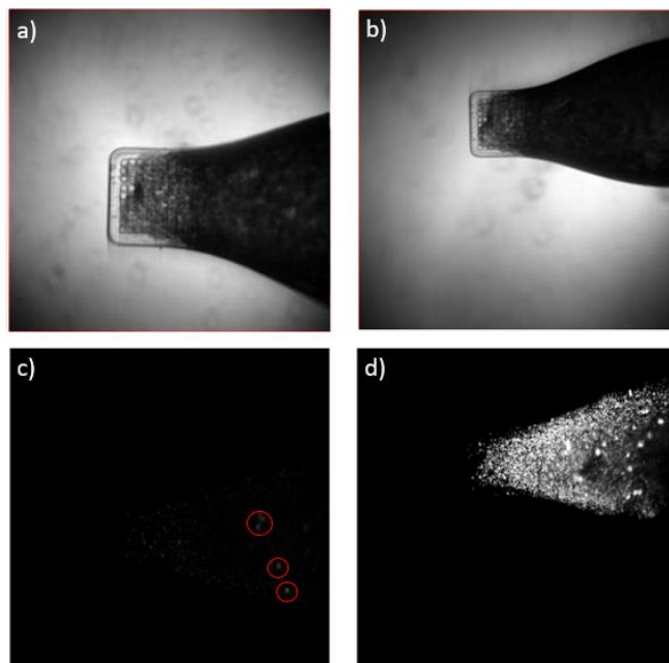


Figure 3.4 Bright field (a,b) and SHG (c,d) images of BaTiO<sub>3</sub> using both the standard Optem objective (a,c) and the custom built objective (b,d). Note, red circles are used to point out the faint particles visible in the SHG image using the Optem objective.

### 3.4 Conclusion and future work

Redesign of the multimodal NLO microscope installed at the beamline at Argonne National Lab was started to allow for epi detection of TPE-UVF and therefore improved signal to noise in this modality. The redesign successfully produced SHG images, but the TPE-UVF signal has yet to be detected with the new beam path. Additionally, a custom-built objective was designed for improved throughput of 1064 nm light. Power readings comparing the custom objective with the standard Optem objective indicate the power throughput was improved by a factor of 3 and therefore an almost 9x increase in SHG intensity, since the SHG signal is proportional to the square of the intensity of the excitation beam. Bright field and SHG images further suggest improved image quality due to the custom objective. While the Optem objective showed faint SHG intensity of BaTiO<sub>3</sub>, the custom objective allowed for saturation of the PMT with the same sample and input power.

Some issues still need to be addressed with the redesign and the custom objective to fully optimize the capabilities of the NLO microscope. Due to the design of the objective, the focal plane for 1064 nm light is shifted ~1 mm from the focal length of 532 nm light. This complicates

imaging as the sample must be placed in different positions for both modalities. Addition of a lens before the scan head should solve this problem, but currently the beam path does not allow for addition of a lens in a kinematic mount to allow for adjustment of the lens for alignment. The new objective also introduces chromatic aberrations when using a white LED as back lighting for bright field imaging using the already-existing collection optics. Since the white LED consists of a combination of light at different visible wavelengths, the custom objective separates these colors out, affecting the quality of the bright field images. Switching from a white LED to a red LED should solve this issue. Additionally, while SHG images were successfully acquired with the redesigned beam path, no TPE-UVF signal was detected. This could be caused by the custom objective, which has the appropriate lens coatings for 1064 nm light but is not optimized for UV light. This may prevent any UV signal from reaching the detector. A new custom designed objective will be developed and optimized for UV detection, though this will sacrifice a significant amount of 1064 nm light throughput. Both objectives will be available for use depending on the imaging modality being used, though the UV-compatible objective will be installed as the new standard objective. This means the SHG modality will no longer be a viable option for protein crystal detection. While SHG is a more reliable approach for protein crystal detection, most general users will not be concerned with identifying samples as crystalline once already at the beamline. For this reason, access to the TPE-UVF modality will be more advantageous for most users.

### 3.5 References

1. Song, J.; Mathew, D.; Jacob, S.A.; Corbett, L.; Moorhead, P.; Soltis, S.M. Diffraction-based automated crystal centering. *J. Synchrotron Radiat.* **2007**, *14*(2), 191-195.
2. Aishima, J.; Owen, R.L.; Axford, D.; Shepherd, E.; Winter, G.; Levik, K.; Gibbons, P.; Ashton, A.; Evans, G. High-speed crystal detection and characterization using a fast-readout detector. *Acta Cryst.* **2010**, *66*, 1032-1035.
3. Sanishvili, R.; Yoder, D.W.; Pothineni, S.B.; Rosenbaum, G.; Xu, S.; Vogt, S.; Stepanov, S.; Makarov, O.A.; Corcoran, S.; Benn, R.; Nagarajan, V.; Smith, J.L.; Fischetti, R.F. Radiation damage in protein crystals is reduced with a micron-sized X-ray beam. *PNAS* **2011**, *108*(15), 6127-6132.
4. Yamamoto, M.; Hirata, K.; Yamashita, K.; Hasegawa, K.; Ueno, G.; Ago, H.; Kumasaka, T. Protein microcrystallography using synchrotron radiation. *IUCrJ* **2017**, *4*(5), 529-539.

5. Wampler, R.D.; Kissick, D.J.; Dehen, C.J.; Gualtieri, E.J.; Grey, J.L.; Wang, H.; Thompson, D.H.; Cheng, J.; Simpson, G.J. Selective detection of protein crystals by second harmonic microscopy. *J. Am. Chem. Soc.* **2008**, 14076-14077.
6. Madden, J.T.; DeWalt, E.L.; Simpson, G.J. Two-photon excited UV fluorescence for protein crystal detection. *Acta Crystallogr. D. Biol. Crystallogr.* **2011**, 67(10), 839-846.
7. Closser, R.G.; Gualtieri, E.J.; Newman, J.A.; Simpson, G.J. Characterization of salt interferences in second-harmonic generation detection of protein crystals. *J. Appl. Crystallogr.* **2013**, 46(6), 1903-1906.
8. Madden, J.T.; Toth, S.J.; Dettmar, C.M.; Newman, J.A.; Oglsebee, R.A.; Hedderich, H.G.; Everly, R.M.; Becker, M.; Ronau, J.A. Buchanan, S.K.; Cherezov, V.; Morrow, M.E.; Xu, S.; Ferguson, D.; Makarov, O.; Das, C.; Fischetti, R.; Simpson, G.J. Integrated nonlinear optical imaging microscope for on-axis crystal detection and centering at a synchrotron beamline. *J. Synch. Rad.* **2013**, 20, 531-540.
9. Scarborough, N.M.; Godaliyadda, G.M.D.P, Ye, D.H.; Kissick, D.J.; Zhang, S.; Newman, J.A.; Sheedlo, M.J.; Chowdhury, A.U.; Fischetti, R.F.; Das, C.; Buzzard, G.T.; Bouman, C.A.; Simpson, G.J. Dynamic X-ray diffraction sampling for protein crystal positioning. *J. Synchrotron Rad.* **2017**, 24, 188-195.

## **CHAPTER 4. DEPTH OF FIELD EXTENSION FOR HIGH THROUGHPUT CRYSTAL SCREENING USING A CUSTOM MICRORETARDER ARRAY**

### **4.1 Introduction**

The generation of high-resolution structures of macromolecules is crucial to understanding the function of proteins and to inform on rational drug design. X-ray diffraction has long been considered the gold standard for macromolecular structure determination. However, this approach greatly depends on the ability to grow high quality crystals prior to diffraction. Currently, the crystallization process is time consuming, often requiring multiple crystallization trials in order to optimize protocols for producing high quality protein crystals. Additionally, verification of successful crystallization protocols requires high-throughput platforms capable of high-speed data acquisition times. Fluorescence imaging techniques are commonly used for identifying the presence of protein crystals. Methods such as UV fluorescence and two-photon excited UV fluorescence (TPE-UVF) rely on the intrinsic fluorescence of most proteins, while trace-labeled fluorescence can be used to detect proteins lacking the amino acid tryptophan.<sup>1-3</sup> Though these techniques have been successfully used for crystal screening, they are limited in selectivity and sensitivity, often generating false positives from aggregate proteins that also produce intrinsic fluorescence signals or from unbound fluorophores.<sup>4-5</sup>

Second harmonic generation has been demonstrated as an effective tool for high-throughput crystal screening of proteins.<sup>6</sup> This technique is advantageous in crystal screening due to the high selectivity to noncentrosymmetric crystalline materials and therefore has little contribution from non-crystalline materials, such as aggregate proteins. Commercially available instruments exist for detecting the SHG signal of protein crystals in 96-well plates.<sup>7</sup> However, this technique is limited by the narrow depth of field (DoF) achievable by conventional approaches, leading to extended data acquisition times and ultimately restricting the throughput of such methods.

Significant work has been done to study methods of extending the DoF in imaging techniques. Reducing the numerical aperture (NA) by using a narrow beam can be used to decrease the tightness of the focal spot and therefore increase the DoF, but at the cost of decreased resolution.<sup>8</sup> Wave-front shaping approaches offer a potential solution to extending the depth of

field by increasing the axial point-spread-function of beams. One method of wave-front shaping employs a phase mask to act as an optical power apodizer in order to extend the DoF, but this method results in a 50% reduction in power at the sample plane.<sup>9</sup> Axicons can also be used for DoF extension by converting a Gaussian beam shape to a Bessel beam.<sup>10</sup> However, this approach is difficult to retrofit into already existing beam paths due to challenges in aligning the axicon. The field of microscopy would greatly benefit from an improved, simple approach for extending the DoF.

In an effort to address issues concerning high-throughput crystal screening, a custom designed, 1-inch microretarder array ( $\mu$ RA) was created to extend the DoF of imaging systems. The custom design consists of concentric patterns which result in half-wave retardance at all positions in the field of view (FoV). A detailed discussion of the design and theory behind the  $\mu$ RA was previously reported.<sup>11</sup> In brief, the patterned  $\mu$ RA results in axially offset foci separated by 70  $\mu$ m, extending the depth of field by this same distance.

In this work, the potential of using the  $\mu$ RA for extending the DoF and improving high throughput crystal screening was evaluated using different samples. Barium titanate ( $\text{BaTiO}_3$ ), ritonavir crystals, and tetragonal lysozyme crystals were all imaged with and without the  $\mu$ RA to provide a direct comparison between the extended DoF approach and conventional z-scanning. Analysis of multiple samples demonstrated the wide variety of applications that could potentially benefit from this approach. Further work was done to evaluate the capability of imaging large batch crystal trials. These results indicate that the  $\mu$ RA improves the overall data acquisition time by a factor of 3 while also detecting more crystal hits than conventional approaches. The small size of the  $\mu$ RA allows for easy retrofitting into already existing beam paths and provides a promising alternative to conventional imaging methods.

## 4.2 Methods

### 4.2.1 $\text{BaTiO}_3$ sample preparation

$\text{BaTiO}_3$  nanoparticles purchased from Sigma-Aldrich were prepared by immobilization in poly(ethylene glycol) (PEG) with a thickness of 1 mm. Prior to immobilization, the  $\text{BaTiO}_3$  nanocrystals were suspended in deionized water at 1 % wt/wt with 30 minutes sonication to ensure even distribution. The PEG solution was prepared in 1 mL of water at 50% wt/wt and was heated to 75 °C to completely melt the PEG. The PEG solution was combined with 100  $\mu$ L of the  $\text{BaTiO}_3$

nanoparticle suspension and was then sonicated for 1 minute. The PEG-BaTiO<sub>3</sub> mixture was spread on a glass slide and allowed to solidify into a thin film at room temperature.

#### 4.2.2 Ritonavir crystal growth

Ritonavir crystals were prepared using a hydraulic press (Atlas Manual Hydraulic Press 15) to form a sandwiched ritonavir-copovidone amorphous solid dispersion (ASD) thin film. The thin films were prepared with 50-60 mg of ASD powder spread out on two circular pieces of aluminum foil. The hydraulic press chamber was heated to 115 °C for 5 minutes and was compressed at a pressure of 4 tons for 10 additional minutes. The temperature was cooled back to 65 °C and pressed at 4 tons again for another 10 minutes. The ASD film was cooled to room temperature. Ritonavir crystals were grown in the films at room temperature under controlled humidity for 48 hours.

#### 4.2.3 Crystallization and preparation of tetragonal lysozyme

Following a protocol adapted from Yaoi, M. et al, tetragonal lysozyme crystals were prepared in a 96-well plate.<sup>12</sup> Chicken egg-white lysozyme purchased from Sigma-Aldrich was used to prepare a 12.5 mg/mL solution in nanopure water. To crystallize the lysozyme, 1 µL of protein solution was combined with 1 µL NaCl-acetate protein buffer solution in a small well and 100 µL of protein buffer was added to the large well to produce protein crystals via the sitting drop method. The well plate was sealed with tape overnight to allow for proper vapor diffusion. Traditionally, tetragonal lysozyme does not produce a strong SHG signal. Previous work has shown the validity of using intercalating dyes to increase the SHG signal of high symmetry crystals.<sup>13</sup> After crystallization, malachite green oxalate salt (MG) purchased from Sigma-Aldrich and prepared in ethyl ethanoate was intercalated into the lysozyme crystals by adding 1 µL of 500 µM dye solution to each well containing protein crystals. The ethyl ethanoate was allowed 10 minutes to evaporate off prior to SHG imaging.

#### 4.2.4 SHG measurements

All SHG images were acquired using the Formulatrix SONICC multimodal nonlinear optical imaging microscope. BaTiO<sub>3</sub> nanoparticles, ritonavir crystals, and tetragonal lysozyme crystals were all imaged using the SONICC instrument to evaluate the capability of the custom



designed  $\mu$ RA for extending the depth of field for high throughput crystal screening. The  $\mu$ RA, the design of which is shown in Figure 5.1, was placed just before the sample plane in the instrument and was easily fitted into the existing beam path by installing it into the existing objective. Images were acquired with and without the  $\mu$ RA in the beam path to provide a comparison between this method and conventional imaging methods. All images were analyzed in ImageJ. Note that a full description and analysis of the design of the  $\mu$ RA was previously published.<sup>11</sup>

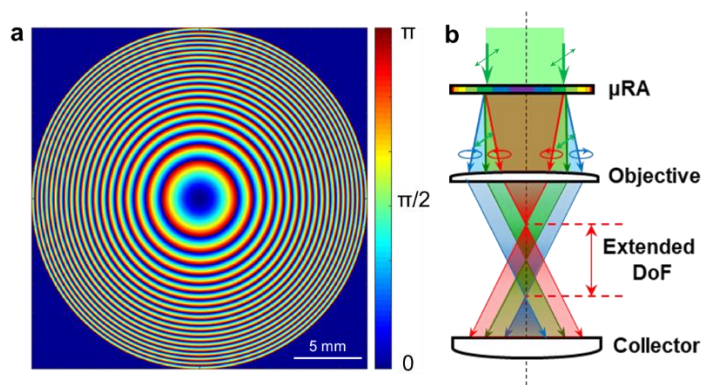


Figure 4.1 a) Custom designed pattern of  $\mu$ RA for depth of field extension using 1064 nm light.  
b) Schematic depicting the principle of depth of field extension by polarization wavefront shaping, where arrows indicate different polarization states of light.

### 4.3 Results

#### 4.3.1 Imaging of BaTiO<sub>3</sub> nanoparticles

SHG imaging of BaTiO<sub>3</sub> nanoparticles provided an initial study for assessing the performance of the  $\mu$ RA for extending the DoF. BaTiO<sub>3</sub> nanoparticles are commonly used as a standard for assessing the performance of SHG microscopes and therefore provide a useful model system for proof-of-concept measurements using the custom designed  $\mu$ RA. SHG images of the BaTiO<sub>3</sub> nanoparticles were acquired with and without the  $\mu$ RA installed in the beam path, the results of which are shown in Figure 5.2. As the figure indicates, images were acquired at multiple z-positions, representing traditional methods which use a z-scan approach in order to capture the entire sample and spanning a distance of 160  $\mu$ m. In the images a-d, different BaTiO<sub>3</sub> nanoparticles were visible in different slices of the z-scan, demonstrating that multiple images were needed in order to detect all of the BaTiO<sub>3</sub> nanoparticles. The z-projection of the four SHG images acquired

is shown in 2e, with the color coding corresponding to particles visible in the different z-planes. The  $\mu$ RA was then placed in the beam path and another SHG image was acquired of the same FoV of the BaTiO<sub>3</sub> nanoparticles, shown in 2f. Comparing the SHG image with the  $\mu$ RA in place to the z-projection showed that the  $\mu$ RA is capable of capturing all of the nanoparticles visible in the z-projection, but with only one image instead of four needed. These results suggest that data acquisition time could be reduced by a factor of four when using the  $\mu$ RA to extend the DoF.

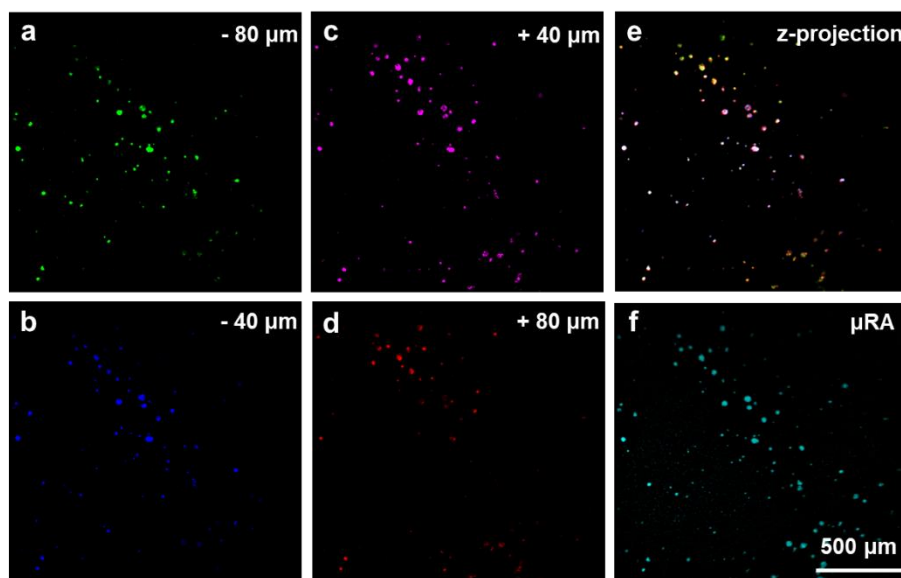


Figure 4.2 a-d) SHG images of BaTiO<sub>3</sub> nanoparticles at different z-planes. e) Summation of SHG images in (a-d). f) Single SHG image of BaTiO<sub>3</sub> nanoparticles with the  $\mu$ RA in the beam path, depicting the same field-of-view as shown in (a-d).

#### 4.3.2 Imaging of ritonavir crystals

Further experiments were conducted on ritonavir crystals grown in a copovidone matrix, comparing the extended DoF approach to the conventional z-scan method. Results for these experiments can be seen in Figure 5.3. Multiple SHG images at different z-plans were taken of the ritonavir crystals and a z-projection was produced from this stack of images, shown in Fig. 5.3a. A single SHG image of the same FoV of ritonavir crystals was acquired with the  $\mu$ RA in place for extended DoF and is shown in Fig. 5.3b. For a direct comparison between the two approaches, an overlay of both results was made and is shown in Fig. 5.3c. In the overlay, the pixels appearing yellow in color show the crystals that were detected by both methods. It should be noted that some pixels shown are green in color, representing crystals detected using the  $\mu$ RA but not by the z-

scanning approach. A possible explanation for this could be the polarization dependence of the SHG intensity detected as a result of crystal orientation. Placing the  $\mu$ RA in the beam path changes the polarization state of the excitation light from linear to circular. Whereas linearly polarized light would cause the crystals stretching perpendicular to the polarization state of the light to have a negligible contribution to the SHG signal, the SHG intensity of the crystals becomes more uniform upon excitation with circularly polarized light.

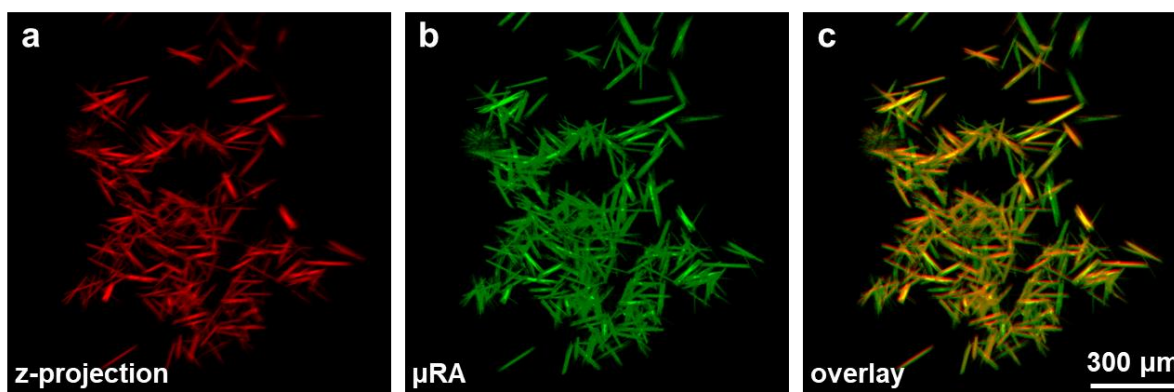


Figure 4.3 A series of SHG images of ritonavir crystals depicting a) the z-projection of images acquired through a z-scan, b) a single image of the same crystals and field-of-view acquired with the  $\mu$ RA in place and c) an overlay of the two to show the differences detected by the two methods.

#### 4.3.3 Imaging of tetragonal lysozyme crystals

To extend the application of the extended DoF approach further, experiments were conducted using tetragonal lysozyme crystals. High-throughput crystal screening is important in the field of structural biology. Therefore, verifying the success of this approach for detecting protein crystals is necessary for evaluating the universality of extending the DoF. Due to the high symmetry of tetragonal lysozyme, these crystals do not produce a strong SHG signal. For this reason, malachite green (MG) was intercalated into the crystals to enhance the SHG signal. The SHG images acquired via z-scanning and extended DoF are summarized in Figure 5.4. Three SHG images were acquired at different z-planes, shown in Fig. 5.4a-c, and were used to generate the z-projection shown in Fig. 5.4d. A total z distance of 300  $\mu$ m was covered in the z-scan. Single SHG images with the  $\mu$ RA in place were acquired using the same exposure and twice the exposure used during the z-scan, shown in Fig. 5.4e and f, respectively. Note that the exposure time was doubled

to provide greater signal to noise and improve visualization of crystals with a weaker SHG signal. As the images show, all of the crystals visible using z-scanning were also visible using the  $\mu$ RA for extended DoF. In fact, some crystals appeared brighter in the extended DoF image than in the z-projection, as shown by the yellow and red circles. Again, this is most likely due the orientation dependence of SHG signals previously discussed.

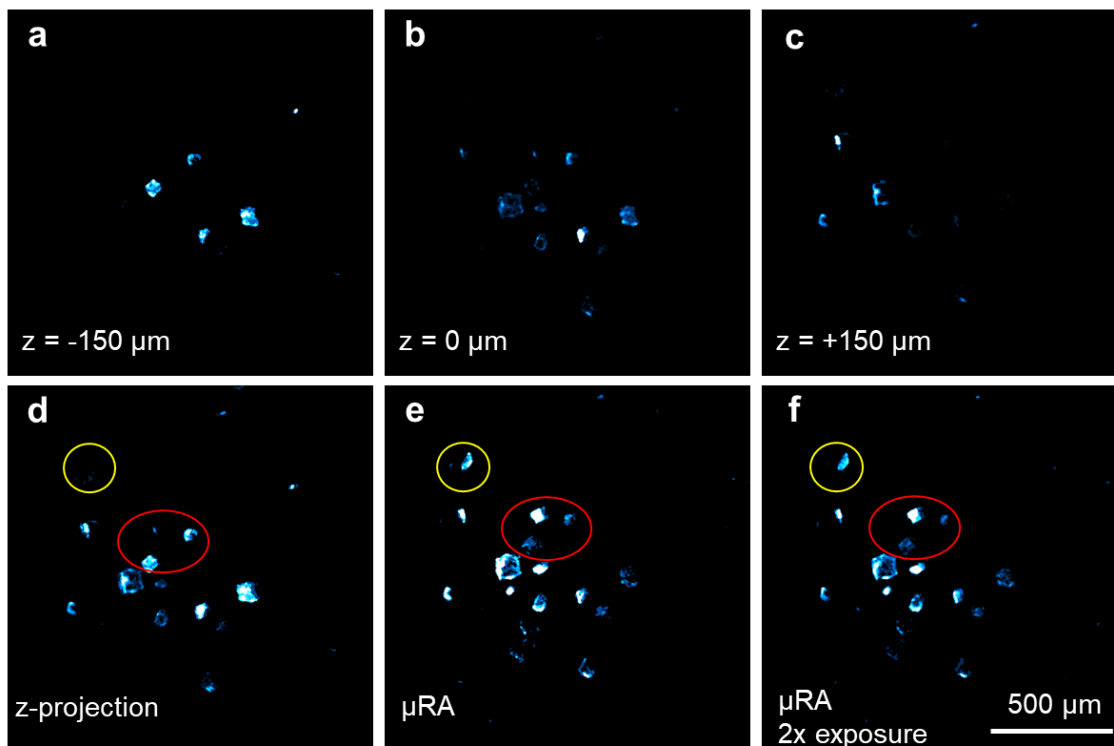


Figure 4.4 a-c) SHG images of tetragonal lysozyme crystals with intercalated malachite green dye at different z-planes d) Z-projection of SHG images shown in (a-c). e-f) SHG images of the same sample and same field-of-view with the same exposure time (e) and double exposure time (f).

#### 4.3.4 High-throughput crystal screening

The motivation behind this work was to improve high-throughput crystal screening by decreasing the total acquisition time required to obtain a full set of images that can identify all present crystals. In an effort to assess the improvement achieved by extending the DoF using a custom  $\mu$ RA, large-batch crystal screening experiments were conducted to compare this approach with conventional screening methods. A total of 7 different crystal wells were imaged both using

a z-scan approach covering a distance of 4 mm and an area of 20.25 mm<sup>2</sup> and using the extended DoF approach. While z-scanning the wells required a total of 96 minutes for data acquisition, the extended DoF resulted in nearly a 3x faster data acquisition time of 34 minutes. Additionally, a particle counting algorithm was used to count the number of crystals detected in each well for each method, the results of which are summarized in Table 5.1. As the data show, an average of 4.64% more crystals were detected using the extended DoF method than with conventional z-scanning. This demonstrates that not only does using the  $\mu$ RA for DoF extension result in a significant decrease in data acquisition, but also enables the detection of more crystals when compared to conventional SHG imaging methods.

Table 4.1 Comparison of the number of crystal counts detected using the extended DoF method and the conventional SHG imaging method.

	Extended DoF	Conventional	Relative Difference
Well 1	1463	1352	8.21%
Well 2	1281	1226	4.49%
Well 3	1265	1195	5.86%
Well 4	1343	1372	-2.11%
Well 5	1359	1160	17.15%
Well 6	926	1013	-8.59
Well 7	819	763	7.34%
Sum	8456	8081	4.64%

#### 4.4 Conclusions

A custom designed  $\mu$ RA for extending the DoF during SHG imaging was shown to be an effective alternative method for high-throughput crystal screening, resulting in a three-fold increase in data acquisition speed compared to the conventional z-scanning method. A variety of different samples were analyzed using the extended DoF method to verify the validity of this work and to demonstrate the universality of this method to be used in various applications. Furthermore, not only did extending the depth of field reduce the total data acquisition time, but this approach also led to an increase in the total number of crystals detected from a large-batch crystallization

trial. These results all indicate that use of a  $\mu$ RA for extending the depth of field provides a potential solution to the issues faced in high throughput crystal screening. While SHG imaging was the focus of these studies, the custom designed  $\mu$ RA could potentially be used and expanded to other imaging modalities used for crystal screening, leading to a broader impact of this work.

#### 4.5 References

1. Judge, R.A.; Swift, K.; Gonzalez, C. An ultraviolet fluorescence-based method for identifying and distinguishing protein crystals. *Acta Crystallogr. D Biol. Crystallogr.* **2005**, *61*(1), 60-66.
2. Madden, J.T.; DeWalt, E.L.; Simpson, G.J. Two-photon excited UV fluorescence for protein crystal detection. *Acta Crystallogr. D Biol. Crystallogr.* **2011**, *67*(10), 839-846.
3. Forsythe, E.L.; Achari, A.; Pusey, M.L. Trace fluorescent labeling for high-throughput crystallography. *Acta Crystallogr. D* **2006**, *62*(3), 339-346.
4. Vernede, X.; Lavault, B.; Ohana, J.; Nurizzo, D.; Joly, J.; Jacquamet, J.; Felisaz, F.; Cipriani, F.; Bourgeois, D. UV laser-excited fluorescence as a tool for the visualization of protein crystals mounted in loops. *Acta Crystallogr. D Biol. Crystallogr.* **2006**, *62*(3), 253-261.
5. Kim, H.; Choi, H.; Kim, S.; Lee, B.; Choi, Y. Antigen-responsive molecular sensor enables real-time tumor-specific imaging. *Theranostics*, **2017**, *7*(4), 952-961.
6. Wampler, R.D.; Kissick, D.J.; Dehen, C.J.; Gualtieri, E.J.; Grey, J.L.; Wang, H.; Thompson, D.H.; Cheng, J.; Simpson, G.J. Selective detection of protein crystals by second harmonic microscopy. *J. Am. Chem. Soc.* **2008**, *130*(43), 14076-14077.
7. Kissick, D.J.; Wanapun, D.; Simpson, G.J. Second-order nonlinear optical imaging of chiral crystals. *Annu. Rev. Anal. Chem.* **2012**, *4*, 419-437.
8. Martinez-Corral, M.; Javidi, B.; Martinez-Cuenca, R.; Saavedra, G. Integral imaging with improved depth of field by use of amplitude-modulated microlens arrays. *Appl. Opt.* **2004**, *43*(31), 5806-5813.
9. Ojeda-Castaneda, J.; Andres, P.; Diaz, A. Annular apodizers for low sensitivity to defocus and to spherical aberration. *Opt. Lett.* **1986**, *11*(8), 487-489.
10. Dufour, P.; Piche, M.; De Koninck, Y.; McCarthy, N. Two-photon excitation fluorescence microscopy with a high depth of field using an axicon. *Appl. Opt.* **2006**, *45*(36), 9246-9252.
11. Ding, C.; Li, C.; Deng, F.; Simpson, G.J. Axially-offset differential interference contrast microscopy via polarization wavefront shaping. *Opt. Express* **2019**, *27*(4), 3837-3850.

12. Yaoi, M.; Aadachi, H.; Kazufumi, T.; Matsumura, H.; Inoue, T.; Mori, Y.; Sasaki, T. Effects of solution stirring on protein crystal growth. *Jap. J. Appl. Phys.* **2004**, *43*(2), 1318-1319.
13. Newman, J.A.; Scarborough, N.M.; Pogranichniy, N.R.; Shrestha, R.K.; Closser, R.G.; Das, C.; Simpson, G.J. Intercalating dyes for enhanced contrast in second-harmonic generation imaging of protein crystals. *Acta Crystallogr. D Biol. Crystallogr.* **2015**, *71*(7), 1471-1477.

## **CHAPTER 5. POLARIZATION DEPENDENT IMAGING USING A MICRORETARDER ARRAY FOR DISCRIMINATION BETWEEN CRYSTALLINE AND AGGREGATE PROTEINS**

### **5.1 Introduction**

Understanding of a protein's functions relies heavily on the ability to generate high resolution structures of crystalline macromolecules. To generate these high-resolution structures, X-ray diffraction patterns are collected by exposing a crystalline sample to a sufficiently powerful X-ray beam such as a synchrotron or X-ray free-electron laser (XFEL). Access to synchrotron beam sources can be limited by location and demand for beam time, while XFELs are still new and not widely available. In addition to limited access to X-ray sources, XRD experiments are time-consuming and the high-powered X-ray beam often destroys the sample, leading to a limited amount of times a diffraction pattern can be obtained from a sample. For this reason, it is crucial to be able to successfully identify the presence of protein crystals prior to X-ray diffraction experiments. Currently, few methods exist that can reliably detect and confirm the presence of protein crystals in crystallization trials. Specifically for the crystallization of proteins, previous studies have utilized birefringent properties of protein crystals as a way to characterize crystal quality.<sup>1</sup> However, this method produces low contrast images and is not as information rich as other alternative methods.<sup>2</sup> Thus the field of crystallography would greatly benefit from an effective and non-destructive method of characterizing protein crystals.

Second harmonic generation (SHG) microscopy has been shown to be an effective method for imaging protein crystals, as only samples that are non-centrosymmetric in nature will produce a signal.<sup>3</sup> Because of these symmetry requirements, SHG can accurately confirm whether an SHG-active protein sample is crystalline or aggregate, as disordered aggregate protein will not produce an SHG signal while crystalline protein will. However, this means that protein crystals that are centrosymmetric will also be undetectable by SHG, therefore limiting the applicability of this technique.

In cases where proteins cannot be detected by SHG microscopy, two-photon excited UV fluorescence (TPE-UVF) imaging can be used as an alternative method. TPE-UVF relies on the intrinsic fluorescence of proteins for detection.<sup>4</sup> Proteins with aromatic residues, most commonly tryptophan, are detectable by TPE-UVF. Unfortunately, this technique by itself does not allow for



discrimination between crystalline and aggregate protein as both will produce a fluorescence signal and therefore alone cannot be used to confirm the presence of protein crystals prior to diffraction experiments.

Incorporation of polarization measurements into TPE-UVF could provide an alternative approach for discriminating between protein crystals and aggregate protein. For any given polarization state of light, the TPE-UVF of aggregate and crystalline proteins should produce different responses. This difference should allow for discrimination between the two forms. Polarization experiments are often done by implementing an electro-optic modulator (EOM) into the beam path, which allows for the modulation of the phase, frequency, amplitude, or polarization of a beam of light.<sup>5</sup> While effective at modulating the polarization state of light, EOMs are large and therefore difficult to retrofit into already existing beam paths. A simpler method to modulate the polarization of an existing beam path is the placement of smaller half and quarter waveplates into the beam path. Though these optics are much smaller, the optic must be rotated to modulate the polarization between each subsequent image in order to access all polarization states.<sup>6</sup> For this reason, this approach is often time consuming and also introduces  $1/f$  noise to the collected images.<sup>7</sup>

The experimental details of a novel approach for polarization-dependent studies of TPE-UVF using a microretarder array ( $\mu$ RA) are described here. The  $\mu$ RA is a 1-inch liquid crystal polymer optic commercially available from Thorlabs that allows for polarization modulation. A plot of the polarization modulation imprinted on the optic is shown in Figure 5.1. By placing this optic in the rear-conjugate plane of the beam path, the polarization modulation can be spatially encoded across the field of view, which has been validated previously for studies in SHG microscopy for structural analysis of collagen.<sup>8</sup> This method for polarization modulation is advantageous, as the small size of the optic allows for easy installation in already existing beam paths and provides a relatively simple alternative to other polarization modulation approaches. Additionally, only one image is needed to access all polarization states, which decreases the data acquisition time compared to other methods, reducing sources of  $1/f$  noise.

Once images have been collected, Fourier analysis allows for discrimination between protein crystals and aggregate proteins. By utilizing Fourier analysis of the data, the first and second order responses can be isolated and used to calculate the ratio of the circular and linear responses. The proposed method suggests that this ratio can be used to discriminate between

crystalline and aggregate protein. Because crystals will produce a different response than aggregate protein due to angle dependence of the crystal, the two ratios can be used to discriminate between crystalline and aggregate protein. A full description of the theoretical framework for the polarization analysis is reported as well.

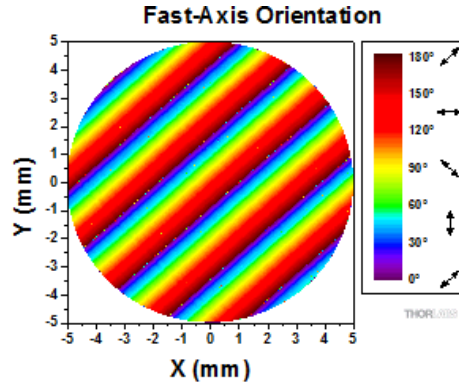


Figure 5.1 Pattern of the microretarder array from Thorlabs; color scale shows the polarization angle across the optic.

## 5.2 Theoretical framework

### 5.2.1 Polarization analysis for TPE-UVF

For the theoretical framework for polarization dependence, the protein crystals will be assumed to be rod-like in nature. Thus, each particle, or crystal, has three Euler angles describing its' orientation ( $\theta, \phi, \psi$ ), where  $\theta$  represents the polar angle,  $\phi$  represents the azimuthal angle, and  $\psi$  represents the twist angle. For simplicity, it is further assumed that the system is dominated by the  $\beta_{zzz}$  molecular tensor element, where  $\beta$  represents the hyperpolarizability. Under these assumptions, only the polar and azimuthal angles will be considered, as the twist angle will not have an effect on the crystal orientation. From these assumptions, only 10 unique polynomial coefficients for this tensor will be non-zero, 5 for horizontally polarized light and 5 for vertically polarized. In its general form, the vector containing the 10 polynomial coefficients can be solved via Equation 5.1, where  $\chi$  is the Jones tensor and  $P$  is a sparse matrix.

$$\vec{A}_n = P \cdot (\vec{\chi}_J^* \otimes \vec{\chi}_J) = \begin{bmatrix} 1 & 0 & 0 & 0 & 0 & 0 & 0 & 0 & 0 \\ 0 & 2 & 0 & 2 & 0 & 0 & 0 & 0 & 0 \\ 0 & 0 & 1 & 0 & 4 & 0 & 1 & 0 & 0 \\ 0 & 0 & 0 & 0 & 0 & 2 & 0 & 2 & 0 \\ 0 & 0 & 0 & 0 & 0 & 0 & 0 & 0 & 1 \end{bmatrix} \cdot \begin{bmatrix} \chi_{nHH}^* \chi_{nHH} \\ \chi_{nHH}^* \chi_{nHV} \\ \chi_{nHH}^* \chi_{nVV} \\ \chi_{nHV}^* \chi_{nHH} \\ \chi_{nHV}^* \chi_{nHV} \\ \chi_{nHV}^* \chi_{nVV} \\ \chi_{nVV}^* \chi_{nHH} \\ \chi_{nVV}^* \chi_{nHV} \\ \chi_{nVV}^* \chi_{nVV} \end{bmatrix} \quad 5.1$$

Multiplication of the nine Jones tensor elements with matrix P connects the experimental observables to the local frame optical properties, resulting in two expressions for  $\vec{A}$ , one for horizontal and one for vertical polarized light, shown in equations 5.2 and 5.3. In these equations,  $\mu$  represents the transition moments,  $\alpha$  represents the two photon absorption tensors, and together  $\mu^* \alpha$  is equal to  $\beta$ . Note that to go from the local frame tensor  $\chi$  to the molecular tensor  $\beta$ , an orientational averaging of a rotation matrix is employed, described in equation 5.4. Here, the constant  $N_b$  represents the bulk number density of fluorophores.

$$\vec{A}_H = \cos^2 \phi \begin{bmatrix} \cos^4 \phi \\ 4 \cos^3 \phi \sin \phi \\ 6 \cos^2 \phi \sin^2 \phi \\ 4 \cos \phi \sin^3 \phi \\ \sin^4 \phi \end{bmatrix} |\mu_z|^2 |\alpha_{zz}|^2 \quad 5.2$$

$$\vec{A}_V = \sin^2 \phi \begin{bmatrix} \cos^4 \phi \\ 4 \cos^3 \phi \sin \phi \\ 6 \cos^2 \phi \sin^2 \phi \\ 4 \cos \phi \sin^3 \phi \\ \sin^4 \phi \end{bmatrix} |\mu_z|^2 |\alpha_{zz}|^2 \quad 5.3$$

$$\vec{\chi}_J^* \otimes \vec{\chi}_J = N_b \langle R \otimes R \otimes R \otimes R \otimes R \otimes R \rangle_{\theta\psi\phi} \cdot \vec{\beta}^* \otimes \vec{\beta} \quad 5.4$$

To explain how the 10 coefficients are obtained, the Jones vector of light at a frequency  $\omega$  for incident polarization angle  $\gamma$ , shown in Equation 5.5, will be used.

$$\vec{e}^\omega = \begin{bmatrix} \cos \gamma \\ \sin \gamma \end{bmatrix} \quad 5.5$$

This vector can be related to the 16 observables shown in Equation 5.4. Only tensor elements with unique polarization contributions will be unique observables. This means that elements with the same index values, regardless of position, will be equal. Considering the tensor elements give in

equation 5.6 reveals that there are only five unique observables, giving rise to the five polynomial coefficients discussed earlier.

$$\vec{\chi}_{nij}^* \otimes \vec{\chi}_{nkl} = \begin{bmatrix} \vec{\chi}_{n00}^* \chi_{n00} \\ \vec{\chi}_{n00}^* \chi_{n01} \\ \vec{\chi}_{n00}^* \chi_{n10} \\ \vec{\chi}_{n00}^* \chi_{n11} \\ \vec{\chi}_{n01}^* \chi_{n00} \\ \vec{\chi}_{n01}^* \chi_{n01} \\ \vec{\chi}_{n01}^* \chi_{n10} \\ \vec{\chi}_{n01}^* \chi_{n11} \\ \vec{\chi}_{n10}^* \chi_{n00} \\ \vec{\chi}_{n10}^* \chi_{n01} \\ \vec{\chi}_{n10}^* \chi_{n10} \\ \vec{\chi}_{n10}^* \chi_{n11} \\ \vec{\chi}_{n11}^* \chi_{n00} \\ \vec{\chi}_{n11}^* \chi_{n01} \\ \vec{\chi}_{n11}^* \chi_{n10} \\ \vec{\chi}_{n11}^* \chi_{n11} \end{bmatrix} \quad 5.6$$

Matrix multiplication of the Jones vector in equation 5.5. with the Jones tensors in equation 5.6 results in Equations 5.2 and 5.3.

The five coefficients can be connected back to the signal intensity via Equation 5.7, where  $\gamma$  is the polarization rotation angle and  $n$  is either H or V. This equation shows how polarization information can be extracted from the signal intensity and vice versa.

$$I_n(\gamma) = A_n \cos^4(\gamma) + B_n \cos^3(\gamma) \sin(\gamma) + C_n \cos^2(\gamma) \sin^2(\gamma) + D_n \cos(\gamma) \sin^3(\gamma) + E_n \sin^4(\gamma) \quad 5.7$$

For this work, analysis will be done in the Fourier domain, so the intensity of the signal must instead be expressed in terms of the Fourier coefficients, shown in Equation 5.8.

$$I_n(\gamma) = a_n + b_n \cos(2\gamma) + c_n \cos(\gamma) + d_n \sin(\gamma) + e_n \sin(2\gamma) \quad 5.8$$

The below matrix Equation 5.9 will be used to map from the polynomial coefficients to the Fourier coefficients via a simple linear transformation and vice versa, using its inverse. Note that for the case of TPE-UVF, the coefficients B and D are assumed to be zero due to the physical origin in the imaginary components of the nonlinear optical response.

$$\begin{bmatrix} a \\ b \\ c \end{bmatrix} = \frac{1}{8} \cdot \begin{bmatrix} 3 & 1 & 3 \\ 1 & -1 & 1 \\ 4 & 0 & 4 \end{bmatrix} \cdot \begin{bmatrix} A \\ C \\ E \end{bmatrix} \quad 5.9$$

For detection of a single polarization component of light, the  $A$  coefficient corresponds to the parallel polarization with the incident fields, while  $E$  corresponds to the contribution from cross-polarized light. Therefore, the linear response is equal to the sum of the  $A$  and  $E$  coefficients. In turn, the circular contribution interacts with all three coefficients. With this knowledge, a transformation matrix can be used that allows for linear contributions from  $A$  and  $E$  and circular contributions from all three coefficients, shown in Equation 5.8. The  $1/4$  scaling factor comes from the 4<sup>th</sup> power scaling of the coefficients, shown previously in Equation 5.7. Equation 5.10 can be used to map the polynomial coefficients to the two-photon fluorescence cross-section via a transformation matrix.

$$\begin{bmatrix} \sigma_{LP} \\ \sigma_{CP} \end{bmatrix} = \begin{bmatrix} 1 & 0 & 1 \\ 1/4 & 1/4 & 1/4 \end{bmatrix} \cdot \begin{bmatrix} A \\ C \\ E \end{bmatrix} \quad 5.10$$

A ratio of  $\sigma_{LP}$  and  $\sigma_{CP}$  produces the desired ratio of circular to linear dichroism for discrimination between crystalline and aggregate protein.

### 5.3 Methods

#### 5.3.1 Sample preparation

Tryptophan solution was prepared at a concentration of 15 mg/mL in ultrapure water. The solution was heated at 80 °C while stirring for 15 minutes to ensure the tryptophan was fully dissolved. Tryptophan crystals were also imaged by placing the crystals on a glass slide. These crystals were crushed via mortar and pestle to make a more uniform sample. Lyophilized lysozyme purchased from Sigma Aldrich was imaged on glass slides as well.

#### 5.3.2 Data acquisition

A commercially available liquid crystal polymer  $\mu$ RA was purchased from Thorlabs with a wavelength range of 350-700 nm to allow for use with 532 nm light. All TPE-UVF images were acquired in the epi direction using a Formulatrix SONICC system. Calibration of the  $\mu$ RA was performed by imaging the one-photon fluorescence of a solution of rhodamine 6G. A polarizer was placed in the beam path prior to the objective and rotated until the fluorescence signal from the sample was minimized. The calibration image acquired in this way was used to calculate the polarization angle at each point on the field of view. Images for polarization analysis of tryptophan

solution, tryptophan crystals, and lyophilized lysozyme were acquired with and without the  $\mu$ RA in the beam path. A 3D-printed mount was custom made to hold the  $\mu$ RA and quarter-wave plate, allowing for both optics to be placed in the rear conjugate plane of the beam path. The quarter waveplate allowed for half wave retardance at 532 nm instead of quarter wave retardance with the  $\mu$ RA alone. All images were acquired with an excitation beam of 532 nm at a max power of 100 mW. The z position of the sample was adjusted after addition of the  $\mu$ RA to refocus the sample, as the optic resulted in a shift in the focal plane. A schematic of the instrument with the  $\mu$ RA installed is shown in Figure 5.2.

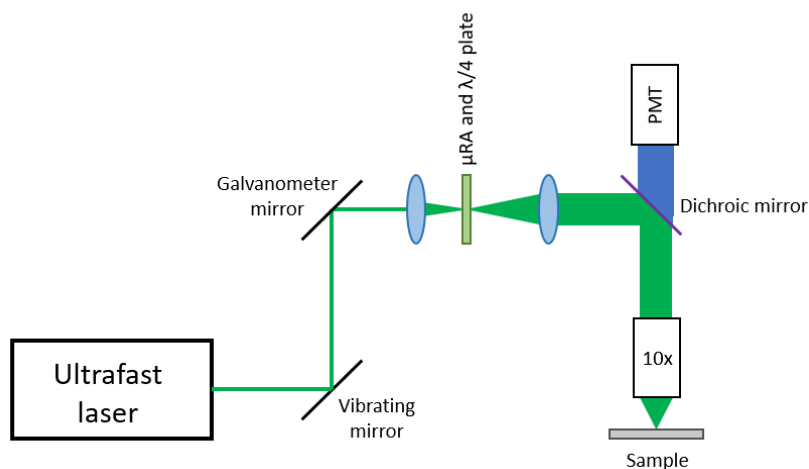


Figure 5.2 Schematic of the beam path for epi TPE-UVF with a  $\mu$ RA installed in the rear conjugate plane.

### 5.3.3 Data analysis

All data analysis was performed using MATLAB. Spatial Fourier analysis was used to isolate the first and second harmonic components from the acquired images, as it is hypothesized that a ratio of these two values will yield the ratio of the circular to linear dichroism which can inform on structure information of the sample. In the data analysis software, a fast Fourier transform was performed on the images of the uniform solution of tryptophan and the resulting peaks in spatial frequency were identified by the script. The identified peaks were then used as a mask to analyze all other data. The first and second harmonic components were used to extract the Fourier coefficients and from there the polynomial coefficients using the math detailed in the previous section.

## 5.4 Results and discussion

TPE-UVF images of the three samples (tryptophan solution, tryptophan crystals, and lyophilized lysozyme) were acquired with and without the  $\mu$ RA installed in the beam path, the results of which are shown in Figure 5.3. As the images show, there is a clear modulation of polarization across the field of view, demonstrated by the faint striping pattern seen in the images taken with the  $\mu$ RA in place.

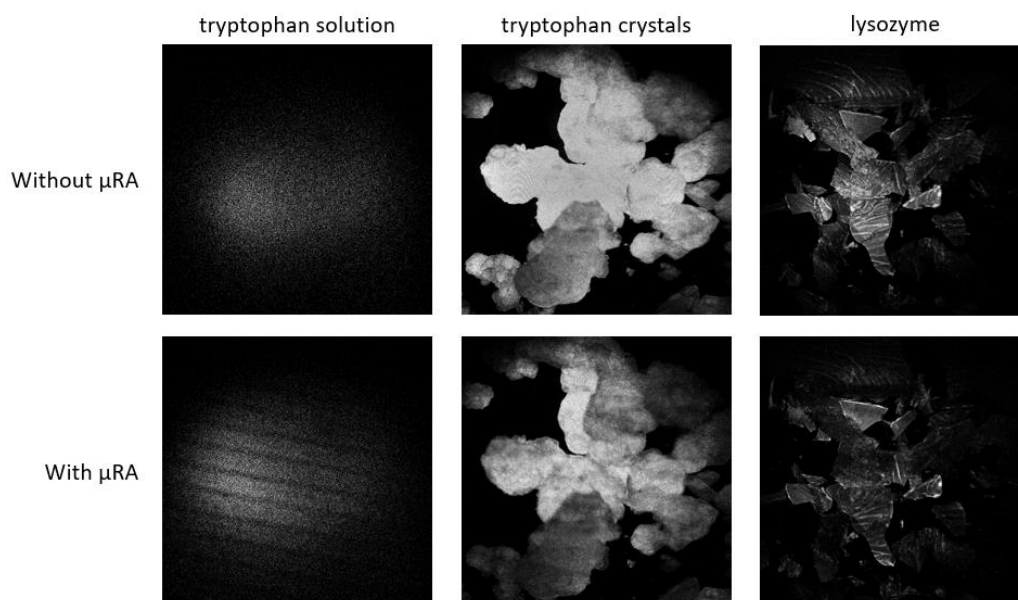


Figure 5.3 TPE-UVF images of tryptophan solution, tryptophan crystals, and lyophilized lysozyme without and with the  $\mu$ RA installed in the beam path.

A Fourier transform was performed on the acquired images, with an example of the resulting Fourier transform of the tryptophan solution shown in Figure 5.4. The first and second harmonic peaks are circled in red and green, respectively. These peaks were used to extract the polynomial coefficients and in turn calculate the ratio of the response to circular versus linear polarized light, the results of which are shown in Table 5.1. Multiple fields of view were analyzed to test the reproducibility of the data analysis software. It should be noted that only the results for the analysis of the tryptophan solution data are reported. When the Fourier analysis approach was applied to the images acquired of the tryptophan crystals and lyophilized lysozyme, the peaks were unable to be extracted due to a large DC component (i.e. the central peak in the Fourier transform) that obscured the first and second harmonic peaks. The ratios appear to be fairly reproducible

within the same sample, but a comparison with other samples would provide a clearer indication of the reproducibility of this approach.

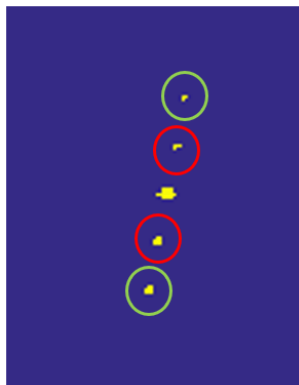


Figure 5.4 Fourier transform of tryptophan solution image, with the first and second harmonic peaks circled in red and green, respectively.

Table 5.1 Results of the Fourier transform of images acquired of tryptophan solution, calculating the ratio of circular to linear polarized light.

FoV	LP	CP	Ratio
1	0.8508	0.6100	0.7169
2	0.8078	0.5802	0.7181
3	1.1636	0.7507	0.6451
4	1.4195	0.8732	0.6151
5	0.8397	0.6285	0.7485

## 5.5 Conclusions and future work

Use of a commercially available  $\mu$ RA was successfully demonstrated as a means for modulation of polarization states across the field of view. This small, readily available optic was easily retrofitted into an existing beam path and required acquisition of only one image to obtain a full set of polarization states for analysis. Fourier analysis was used to extract information of the polynomial coefficients from the acquired images and therefore used to calculate the circular to linear dichroism ratio. As of yet, this technique has not been applied to protein crystals, so the validity of this approach for discriminating between crystalline and aggregate protein has not been shown. While this work demonstrates the ability to modulate the polarization of light across the



field of view using the microretarder array, and that Fourier analysis can be used to recover the polynomial coefficients, more work needs to be done to determine whether the results obtained are valid and if this approach can be applied to protein crystals. Furthermore, there is a phase matching issue that still needs to be addressed, in that

## 5.6 References

1. Owen, R.L., Garman, E. A new method for predetermining the diffraction quality of protein crystals: using SOAP as a selection tool. *Acta. Cryst. D.* **2005**, *61*, 130-140.
2. Kissick, D.J., Gualtieri, E.J., Simpson, G.J. Nonlinear optical imaging of integral membrane protein crystals in lipidic mesophases. *Anal. Chem.* **2010**, *82*, 491-497.
3. Wampler, R.D.; Kissick, D.J.; Dehen, C.J.; Gualtieri, E.J.; Grey, J.L.; Wang, H.; Thompson, D.H.; Cheng, J.; Simpson, G.J. Selective detection of protein crystals by second harmonic generation. *J. Am. Chem. Soc.* **2008**, *130*(43), 14076-14077.
4. Madden, J.T.; DeWalt, E.; Simpson, G.J. Two-photon excited UV fluorescence for protein crystal detection. *Acta. Crystallogr. D. Biol. Crystallogr.* **2011**, *67*(10), 839-846.
5. Robertson, N.A.; Hoggan, S.; Mangan, J.B.; Hough, J. Intensity stabilization of an argon laser using an electro-optic modulator – performance and limitations. *Appl. Phys. B* **1986**, *39*, 149-153.
6. Stoller, P.C.; Kim, B.; Rubenchik, A.M.; Reiser, K.M.; Da Silva, L.B. Polarization-dependent optical second-harmonic imaging of rat-tail tendon. *J. of Biomedical Optics* **2002**, *7*(2), 205-214.
7. DeWalt, E.L.; Sullivan, S.Z.; Schmitt, P.D.; Muir, R.D.; Simpson, G.J. Polarization-modulated second harmonic generation ellipsometric microscopy at video rate. *Anal. Chem.* **2014**, *86*(16), 8448-8456.
8. Ulcickas, J.R.W.; Ding, C.; Deng, F.; Simpson, G.J. Spatially encoded polarization-dependent nonlinear optics. *Optics Letters* **2018**, *43*(24), 5973-5976.

## CHAPTER 6. RECOVERY OF SHG SIGNAL AFTER PHOTBLEACHING OF R6G-LABELED LYSOZYME

### 6.1 Introduction

Through the crystallization process, most protein crystals prepared for X-ray diffraction experiments are predominantly composed of water, which occupy interstices within the crystal lattice and help to retain the native protein structure. For this reason, it is logical to expect that dehydrated protein crystals would not retain order due to their fragile nature. Despite this, significant literature exists demonstrating that dehydrated proteins do in fact retain their native lattice structure.<sup>1-3</sup> This makes it possible for X-ray diffraction analysis of dehydration-induced structural reorganization to be performed.<sup>4-5</sup> In some cases, dehydration of samples has been shown to even improve the achieved resolution of diffraction patterns.<sup>6-7</sup> Understanding protein interactions within glassy matrices is of particular importance to the lyophilization process for protein storage, as lyophilizing proteins is a key step in the design of protein formulations.<sup>8</sup> As such, further insight into molecular changes in glassy proteins can provide foundational knowledge of the transition between solubilized protein to a glassy matrix and potentially improve the stability of proteins in the lyophilization process.

Fluorescence recovery after photobleaching (FRAP) is a method commonly used for determining the kinetics of diffusion of fluorescent molecules in tissues and cells.<sup>9</sup> In FRAP, fluorescent molecules are introduced to specific areas of interest within a sample and are then bleached with a high-intensity laser. In cases where the fluorescent molecules are mobile, the bleached molecules will be exchanged with non-bleached molecules in surrounding areas. The time it takes for recovery can be measured and used to identify diffusion constants, interactions, and binding behaviors.<sup>10-12</sup> FRAP measurements are often carried out with confocal and wide-field microscopes.<sup>13-14</sup> Extending FRAP-based measurements to nonlinear optical imaging methods, such as second harmonic generation (SHG) and two-photon excited UV fluorescence (TPE-UVF), could provide a complimentary method to studying protein mobility, as these techniques are commonly used for the detection of protein crystals.<sup>15-16</sup>

In this work, electronic modifications were made to an already existing nonlinear optical (NLO) microscope installed at the synchrotron facilities at Argonne National Laboratory in order to perform FRAP experiments with the system.<sup>17</sup> These modifications allowed for patterned

bleaching of samples using 532 nm light by changing the pattern of scanning of the galvanometer mirror. The main motivation behind this work was to investigate the SHG signal recovery of protein crystals after photobleaching as a function of temperature. Access to the cryo-stream installed at the beamline at the APS provided an opportunity for easy temperature adjustment while simultaneously acquiring SHG images. Samples of R6G-labeled and R6G-intercalated lysozyme crystals were bleached and SHG images were acquired as the temperature of the cryo-stream was increased in order to measure the SHG signal recovery after photobleaching. Plotting of the recovered SHG intensity revealed a possible structural transition point around 200 K, which is consistent with reported literature.<sup>18</sup> This transition point is attributed to a secondary glass transition associated with polymer backbone motion, referred to as  $\beta$ -relaxation (CITE).<sup>19</sup>

## 6.2 Methods

### 6.2.1 Sample preparation

Tetragonal lysozyme crystals were grown via the method detailed in Yaoi, M. et al.<sup>20</sup> In brief, chicken egg-white lysozyme purchased from Sigma-Aldrich was used to prepare a 12.5 mg/mL solution in ultrapure water. In a 96-well plate, 1  $\mu$ L of protein solution was combined with 1  $\mu$ L NaCl-acetate buffer solution in a small well and 100  $\mu$ L of the buffer solution was added to the large well. The wells were sealed with tape and crystals were grown overnight via vapor diffusion. To prepare R6G-labeled lysozyme, trace amounts of R6G in solution were added to the crystallization well prior to crystals forming to allow for covalent bonding of the R6G molecules to primary amines in the protein. For intercalating R6G into the lysozyme crystals, 1  $\mu$ L of R6G solution was added to the lysozyme crystals and allowed to intercalate into the crystal lattice for 10 min. Crystals were looped in cryo-loops and flash frozen in liquid nitrogen prior to experiments.

### 6.2.2 Electronics modifications

Modifications were made to the custom electronics package that controls the galvanometer (galvo) mirror to allow for bleaching experiments. These modifications were done by Mark Carlson in the Amy Facility at Purdue University, allowing for a striped scanning pattern during imaging. The software interface that controls the galvo mirror can be seen in Figure 6.1. As the interface shows, the galvo mirror can be adjusted to scan as a chosen number of stripes for a set

number of scans. Phase 1 controls the regular imaging in order to acquire a base image prior to bleaching. Phase 2 controls the bleach step, where the number of ramp steps can be decreased to allow for striping across the field of view, and Phase 3 allows for acquisition of another image post bleach. All values can be changed as needed, depending on the desired amount of bleaching.

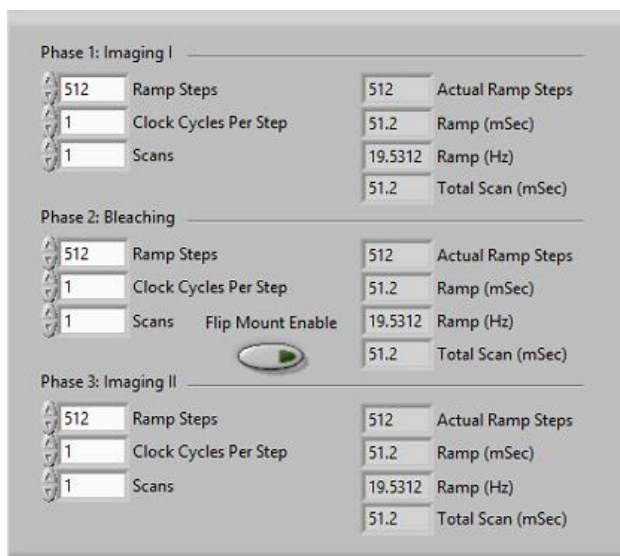


Figure 6.1 Software interface for patterned bleaching using the galvanometer mirror

### 6.2.3 Photobleaching

Photobleaching was performed using the LabView interface for powering the galvanometer mirror. The experiment was set up in a 3-step method: 1) Normal image scanning to acquire a base image of the sample prior to bleaching, 2) Striped scanning for a set number of scans, identified based on how many scans were needed to sufficiently bleach the samples, and 3) Normal imaging scanning again to acquire an image showing whether or not the sample had been sufficiently bleached. All bleaching was done with 532 nm light at the maximum power allowed under cryogenic temperature using a cryo-stream. Samples were bleached repeatedly until stripes were visible in the crystals when SHG images were acquired.

### 6.2.4 Temperature ramp and image acquisition

The temperature ramp experiment was conducted by adjusting the temperature of the cryo-stream in 10-unit increments, from 100 K to 240 K. An SHG image was acquired after each

temperature increase. All SHG images were acquired using 1064 nm light pre- and post-photobleaching with samples in the cryo-stream.

### 6.2.5 Data processing

All images were processed using ImageJ. A line trace was drawn through the crystal and a profile plot was visualized to measure the bleach “depth” of the stripes as a way to determine the recovery of the SHG intensity as temperature was increased. The max and min of the plot were subtracted to provide the depth values. An example of the profile plot is shown in Figure 6.2. All depth values were normalized and plotted as a function of temperature.

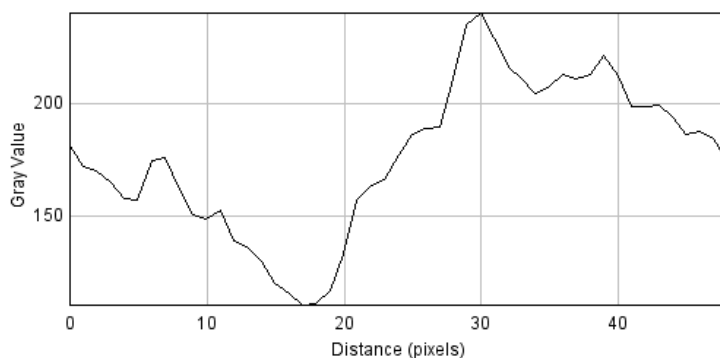


Figure 6.2 Profile plot from SHG image of R6G-labeled lysozyme at 100 K, after photobleaching, for measurement of bleach “depth”.

## 6.3 Results and discussion

### 6.3.1 Photobleaching of lysozyme

Photobleaching was performed on both R6G-labeled and R6G-intercalated lysozyme crystals. The SHG images acquired pre- and post-bleach are shown in Figure 6.3. As the images show, there were clear stripes “bleached” into the crystals, especially the R6G-labeled sample, demonstrating successful photobleaching. Red arrows are shown to help point out the “bleached” stripes. Note that while SHG images were acquired to track the recovery of the SHG intensity, the actual photobleaching was performed using 532 nm light instead of 1064 nm light. Bleaching with 1064 nm was unsuccessful, as no amount of scanning was enough for persistent photobleaching. Additionally, significantly more bleaching was needed for the R6G-intercalated lysozyme sample compared to the R6G-labeled sample. This could be due to the intercalated R6G molecules having

more mobility, since the molecules are not actually bound to the crystal but rather free floating in the crystal lattice.

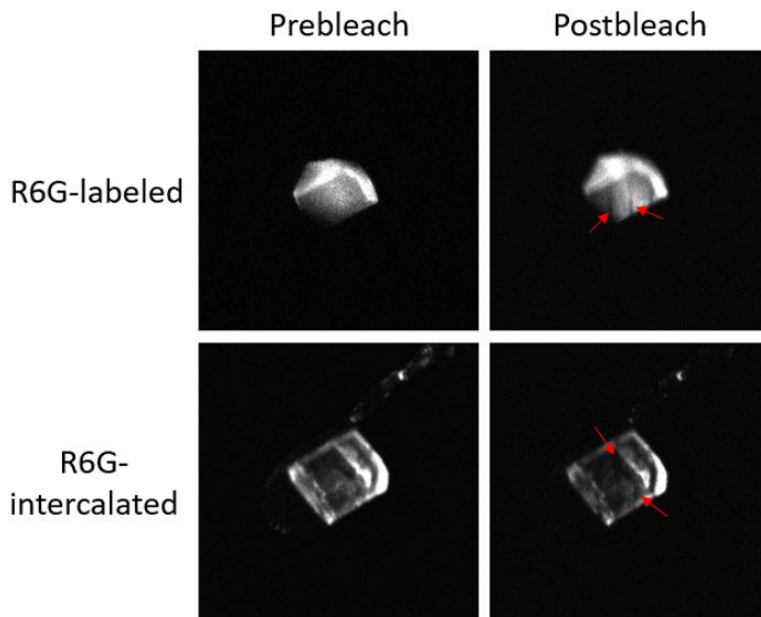


Figure 6.3 SHG images of R6G-labeled and R6G-intercalated lysozyme crystals pre- and post-bleaching, with red arrows shown to point out the striped pattern post bleach.

### 6.3.2 Recovery of SHG intensity as a function of temperature

After sufficient photobleaching of lysozyme crystals was achieved, the temperature of the cryo-stream was adjusted in 10 K increments and SHG images were acquired after each temperature increase. The results for this are shown in Figure 6.4. The recovered SHG signal, reported in terms of normalized stripe “depth”, was plotted against temperature to show how the signal recovery varied with the temperature increase. As the plot in Figure 6.4 shows, there was a significant signal recovery around 200 K for both lysozyme samples. This is significant, but not entirely surprising, as literature reports a transition point at this temperature, below which  $\alpha$ - and  $\beta$ -relaxation processes in glassy proteins converge, where  $\alpha$  represents a primary relaxation process and  $\beta$  corresponds to relaxation associated with polymer backbone motion.<sup>18-19</sup> As this trend was seen for both the R6G-labeled and R6G-intercalated crystals, this suggests that this transition point is a general effect on protein crystals and does not depend solely on protein mobility. Furthermore, the data show that almost complete recovery of SHG signal was observed for the R6G-labeled

sample, but not for the R6G-intercalated sample. This could possibly be that some of the intercalated R6G molecules have moved away from the crystal since they are unbound to the crystal lattice and therefore are not recovered, whereas the covalently bound molecules are still attached to the protein.

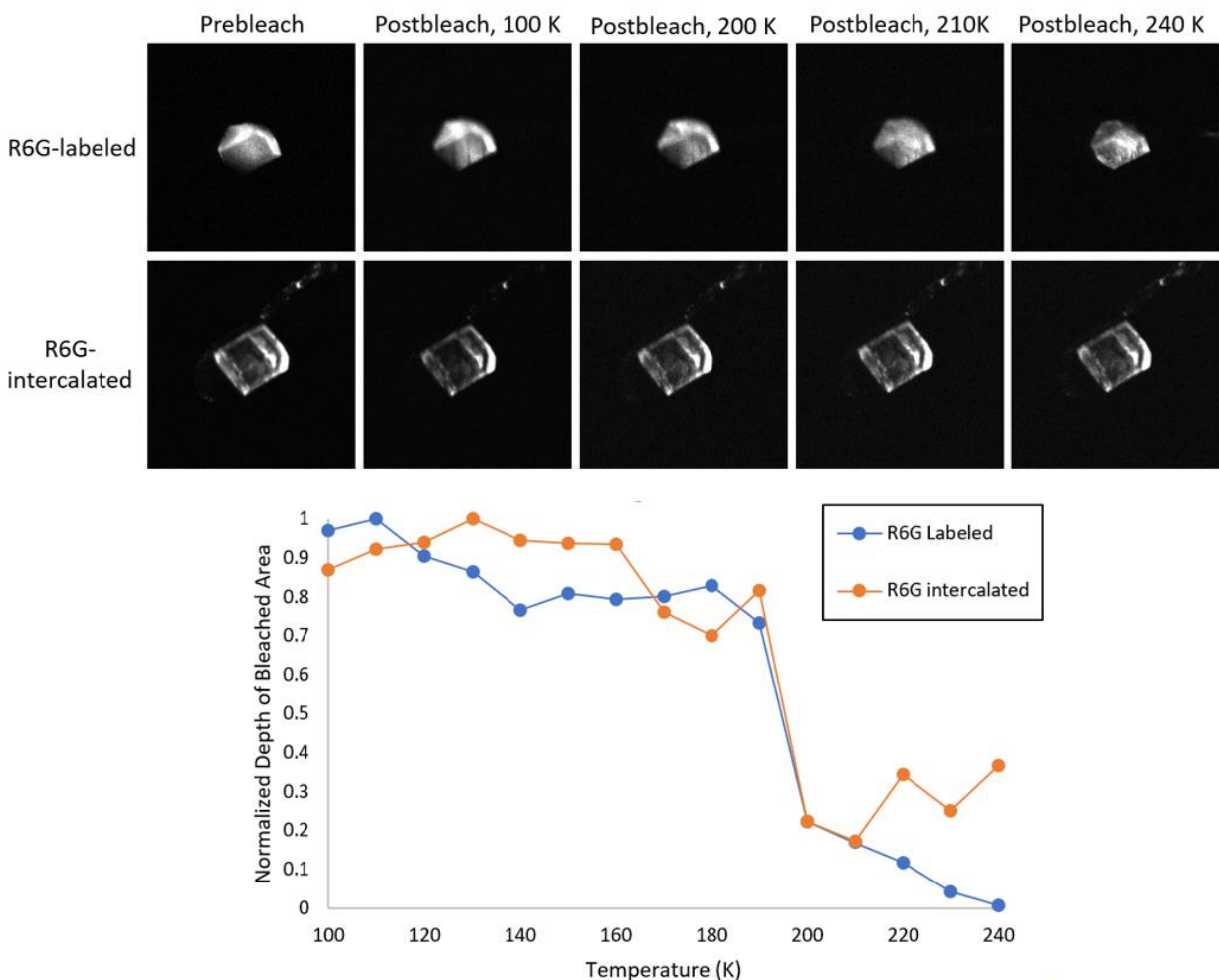


Figure 6.4 SHG recovery after photobleaching of R6G-labeled and R6G-intercalated lysozyme. The temperature of the cryo-stream was increased in 10 K increments and SHG images were acquired after each temperature ramp. The resulting SHG signal recovery is plotted as the normalized depth of bleached stripes vs the temperature of the cryo-stream.

#### 6.4 Conclusions and future work

Preliminary results were obtained to demonstrate the ability to conduct FRAP experiments at the synchrotron source at Argonne National Lab. After photobleaching, the SHG signal was

measured for R6G-labeled and R6G-intercalated lysozyme as a function of temperature. As the temperature was increased, the SHG intensity of both samples was partially recovered starting at around 200 K. This result is interesting as there is a reported glass transition state for water at this same temperature. Furthermore, significantly more bleaching was required to sufficiently bleach the intercalated sample. This finding suggests that unbound dye is more easily able to move and therefore recover signal more quickly than the covalently labeled dye, providing some insight into the mobility of molecules at cryogenic temperatures.

One issue with these experiments was the inability to acquire individual images of each bleach step due to software limitations. Because these images could potentially provide some additional information, software modifications will be made to allow for acquisition of these images, rather than an averaged image for the bleaching step. Additionally, preliminary experiments were intended to use 1064 nm light for photobleaching and imaging, but sufficient bleaching was not achieved with this wavelength of light and instead was done with 532 nm light. To address this concern, photoactivable dyes provide a potential solution to allow for bleaching with a specific wavelength of light. Future work will focus on acquiring X-ray diffraction data post bleaching to investigate the effect on the structure of samples. Once the methodology for conducting the FRAP experiments is optimized, a computational method that has been previously developed for disentangling effects from X-ray induced damage using non-negative matrix factorization will be applied to diffraction data from protein crystals after dehydration.

## 6.5 References

1. Salunke, D.; Veerapandian, B.; Kodandapani, R.; Vijayan, M., Structural transformations in protein crystals caused by controlled dehydration. *J. Biosci. (Bangalore)* **1985**, 8(1-2), 37-44.
2. Nagendra, H.; Sukumar, N.; Vijayan, M., Role of water in plasticity, stability, and action of proteins: the crystal structures of lysozyme at very low levels of hydration. *Proteins: Structure, Function, and Bioinformatics* **1998**, 32(2), 229-240.
3. Harata, K.; Akiba, T., Structural phase transition of monoclinic crystals of hen egg-white lysozyme. *Acta Crystallogr. D Biol. Crystallogr.* **2006**, 62(4), 375-382.
4. Kodandapani, R.; Vijayan, M., Protein hydration and water structure: X-ray analysis of a closely packed protein crystal with very low solvent content. *Acta Crystallogr. D Biol. Crystallogr.* **1993**, 49(2), 234-245.



5. Bell, J. A., X-ray crystal structures of a severely desiccated protein. *Protein Sci.* **1999**, 8(10), 2033-2040.
6. Kuo, A.; Bowler, M. W.; Zimmer, J.; Antcliff, J. F.; Doyle, D. A., Increasing the diffraction limit and internal order of a membrane protein crystal by dehydration. *J. Struct. Biol.* **2003**, 141(2), 97-102.
7. Heras, B.; Edeling, M. A.; Byriel, K. A.; Jones, A.; Raina, S.; Martin, J. L., Dehydration converts DsbG crystal diffraction from low to high resolution. *Structure* **2003**, 11(2), 139-145.
8. *Lyophilization in Pharmaceutical Market Forecast 2019-2029*; Visiongain: 2019.
9. Meyvis, T.K.L.; De Smedt, S.C.; Van Oostveldt, P.; Demeester, J. Fluorescence recovery after photobleaching: a versatile tool for mobility and interaction measurements in pharmaceutical research. *Pharmaceutical Research* **1999**, 16(8), 1153-1162.
10. Ellenberg, J.; Siggia, E.D.; Moreira, J.E.; Smith, C.L. Presley, J.F.; Worman, H.J.; Lippincott-Schwartz, J. Nuclear membrane dynamics and reassembly in living cells: targeting of an inner nuclear membrane protein interphase and mitosis. *J. Cell Biol.* **1997**, 138(6), 1193-1206.
11. Soumpasis, D.M. Theoretical analysis of fluorescence photobleaching recover experiments. *Biophys. J.* **1983**, 41(1), 95-97.
12. Sprague, B.L.; Pego, R.L.; Stavreva, D.A.; McNally, J.G. Analysis of binding reactions by fluorescence recover after photobleaching. *Biophys. J.* **2004**, 86(6), 3473-3495.
13. Meddens, M.B.M.; de Keijzer, S.; Cambi, A. Chapter 4: High spatiotemporal bioimaging techniques to study the plasma membrane nanoscale organization. In Cornea, A. and Conn, P.M., *Fluorescence Microscopy*, **2014**, Academic Press, 49-63.
14. Machan, R.; Foo, Y.H.; Wohland, T. On the equivalence of FCS and FRAP: simultaneous lipid membrane measurements. *Biophys. J.* **2016**, 111(1), 152-161.
15. Wampler, R.D.; Kissick, D.J.; Dehen, C.J.; Gualtieri, E.J.; Grey, J.L.; Wang, H.; Thompson, D.H.; Cheng, J.; Simpson, G.J. Selective detection of protein crystals by second harmonic microscopy. *J. Am. Chem. Soc.* **2008**, 130(43), 14076-14077.
16. Madden, J.T.; DeWalt, E.L.; Simpson, G.J. Two-photon excited UV fluorescence for protein crystal detection. *Acta Crystallogr. D Biol. Crystallogr.* **2011**, 67(10), 839-846.
17. Madden, J.T.; Toth, S.J.; Dettmar, C.M.; Newman, J.A.; Oglsebee, R.A.; Hedderich, H.G.; Everly, R.M.; Becker, M.; Ronau, J.A. Buchanan, S.K.; Cherezov, V.; Morrow, M.E.; Xu, S.; Ferguson, D.; Makarov, O.; Das, C.; Fischetti, R.; Simpson, G.J. Integrated nonlinear optical imaging microscope for on-axis crystal detection and centering at a synchrotron beamline. *J. Synch. Rad.* **2013**, 20, 531-540.

18. Shinyashiki, N.; Yamamoto, W.; Yokoyama, A.; Yoshinari, T.; Yagihara, S.; Kita, R.; Ngai, K.; Capaccioli, S., Glass transitions in aqueous solutions of protein (bovine serum albumin). *J. Phys. Chem. B* **2009**, *113*(43), 14448-14456.
19. Smith, G.D.; Bedrov, D. Relationship between the  $\alpha$ - and  $\beta$ -relaxation processes in amorphous polymers: Insight from atomistic molecular dynamics simulations of 1,4-polybutadiene melts and blends. *J. Polym. Sci. B Polym. Phys.* **2007**, *45*, 627-643.
20. Yaoi, M.; Aadachi, H.; Kazufumi, T.; Matsumura, H.; Inoue, T.; Mori, Y.; Sasaki, T. Effects of solution stirring on protein crystal growth. *Jap. J. Appl. Phys.* 2004,*43*(2), 1318-1319.

## **CHAPTER 7. SHG ENHANCEMENT IN PROTEIN CRYSTALS USING A TETRACYSSTEINE-FLASH TAG IN MALTOSE BINDING PROTEIN**

### **7.1 Introduction**

As protein crystals trend to increasingly smaller sizes and become harder to detect, there is a growing need for new and improved methods for the detection and characterization of protein crystals. Many of the current methods being employed utilize fluorescence imaging techniques, such as covalently bound fluorophores, two-photon excited UV fluorescence (TPE-UVF), and UV fluorescence (UVF). In the case of TPE-UVF and UVF, only proteins with high intrinsic fluorescence can be detected using these methods.<sup>1-3</sup> In addition, these techniques are ineffective for distinguishing between protein crystals and aggregate proteins and can lead to false positives.<sup>4</sup> For proteins that do not exhibit intrinsic fluorescence, covalently modifying proteins with fluorophores will allow for fluorescent imaging. However, studies have shown that the addition of a fluorophore can cause adverse effects to the structure of the protein.<sup>5</sup> The development of a technique to reduce the limitations of currently used methods would be advantageous.

Second harmonic generation (SHG) has been shown as an effective alternative for the detection of protein crystals.<sup>6</sup> SHG is highly selective and sensitive to crystalline material and therefore can readily identify between crystalline and aggregate protein. Previously, work has been done to show the ability of intercalating dyes to provide a contrast enhancement in the SHG signal in an effort to decrease the number of false negatives during crystal screening.<sup>7</sup> However, at millimolar concentrations, these dyes can have a significant effect on the crystallization of the protein.<sup>7</sup> For this reason, a method that allows for lower concentrations of dye would prove more useful. Additionally, due to the specific symmetry requirements of SHG, not all proteins produce a strong SHG signal. The use of a novel tetracysteine-FlAsH tag that produces a fluorescence signal upon dye binding at low concentrations and has the potential to enhance the SHG signal in proteins provides a possible solution to the limitations in protein crystal detection.

The tetracysteine tag consists of a six amino acid sequence, Cys-Cys-X-X-Cys-Cys, where the X's represent any amino acid other than cysteine, but most commonly are proline and glycine due to this motif's high specificity to biarsenic compounds.<sup>8</sup> The biarsenic FlAsH dye will bind covalently to the cysteine residues in the tag and upon binding will result in a fluorescent signal, as shown in Figure 7.1. The small size of this tag is highly attractive, as this will be less likely to

affect the crystallization and function of the protein.<sup>9</sup> In addition, the dye is highly specific to the tag and is capable of nanomolar binding.<sup>10</sup> Because the dye only produces a fluorescent signal when bound, this system also reduces the background signal that often occurs in other methods. Furthermore, addition of this tag to a protein is hypothesized to enhance the SHG signal in proteins with high symmetry and therefore low SHG signal, increasing the application of SHG imaging for the detection of protein crystals. The FAsH dye is similar in structure to lambda dyes which are known to produce a strong SHG signal. This tag also has the added advantage of knowing the specific location of where the dye is binding because the FAsH dye will only bind where the tetracysteine tag is located.

This tetracysteine tag system was incorporated into maltose binding protein (MBP), a chaperone protein that is used to help facilitate purification and crystallization of other proteins.<sup>11</sup> By using this specific protein, a new construct enabling the detection of both SHG and fluorescence while minimizing the unwanted affects to the target protein will be developed. Not only will this system serve as a protein crystal detection tool, but, due to the nature of MBP, will also improve the crystallization of the target protein. This system served as a proof of concept to demonstrate that the FAsH-tetracysteine tag can be incorporated into a specific protein of interest with minimal effects. In cases where the addition of the entire MBP construct as a tag is not ideal, only the tetracysteine tag would need to be engineered into the protein for detection of crystals to be possible.

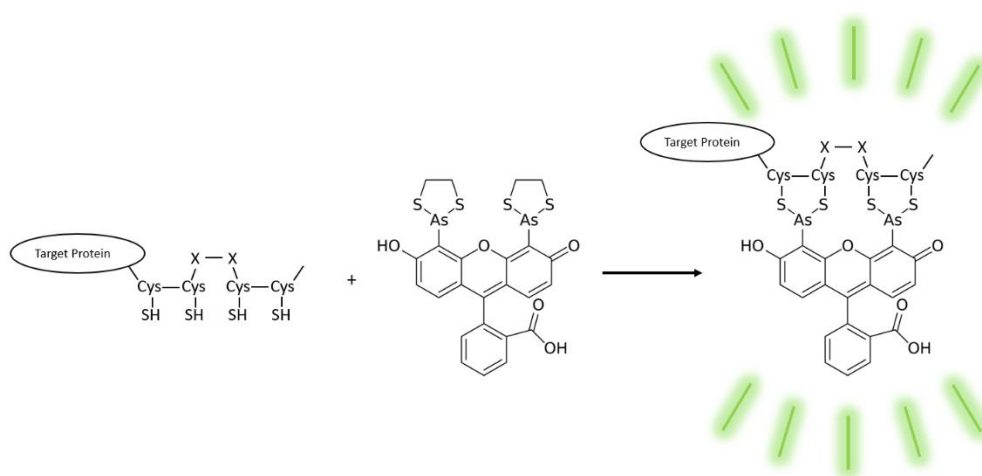


Figure 7.1 Mechanism of FAsH dye binding to a tetracysteine tag incorporated into the target protein.

## 7.2 Methods

### 7.2.1 Expression and crystallization of MBP

The vector used for expression of the MBP-tetracysteine construct was obtained from GenScript USA. Expression, purification, and crystallization of the construct was performed by the Das group at Purdue University. Purification was done using amylose affinity chromatography and gel filtration. The protein was concentrated down to a concentration of 16.5 mg/mL. The protein was then crystallized in 4% Tacsimate pH 6.0, 12% w/v polyethylene glycol 3350 via sitting drop/vapor diffusion using 1  $\mu$ L of protein and 1  $\mu$ L of mother liquor. The protein was left to crystallize for two weeks. Images of the protein crystals were obtained using a Lecia MZ 95 microscope with 4x magnification.

### 7.2.2 Labeling with FAsH dye

The TC-FAsH II In-Cell Tetracysteine Tag Detection Kit used for labeling of the protein was obtained from Thermo-Fisher Scientific. The biarsenical dye was diluted from an original concentration of 2 mM to 500 nM using the same mother liquor used for protein crystallization. Previous work has been done using this concentration of dye with positive results.<sup>9</sup>

### 7.2.3 Fluorimetry measurements

Fluorimetry measurements were done to confirm the presence of the tetracysteine tag in the MBP construct. Measurements were conducted using an Edinburgh Instruments FLS980 Steady State Fluorescence Spectrometer. Samples of MBP with FAsH dye were prepared with equal concentrations of 1  $\mu$ M. The experimental conditions were set to scan from 518 nm-598 nm for comparing the fluorescence intensities in the presence and absence of the FAsH dye and from 527-529 nm for kinetic studies, with a step size and slit width of 1 nm and a dwell time of 5 s.

### 7.2.4 Acquisition of SHG images

SHG images of the protein crystals before and after addition of the dye were obtained using a commercial SONICC (second-order nonlinear optical image of chiral crystals) microscope from Formulatrix, Inc. This system uses a Fianium FemtoPower laser at a 51 MHz repetition rate

and 166 fs pulse width. A laser power of 350 mW and an exposure time of 1 second were used. After images of the protein crystals were acquired, 1  $\mu$ L of 500 nM biarsenic dye was added to the protein crystals. Images were then obtained multiple times over the course of one hour to determine the SHG intensity enhancement factor due to the binding of the dye. Fluorescent images of the protein crystals with dye added were acquired using an Olympus BX-51 Optical Microscope with 10x magnification, courtesy of the Research Instrument Center at Purdue University.

## 7.3 Results and discussion

### 7.3.1 Fluorescence studies

To confirm successful engineering of the tetracysteine tag into MBP, fluorescence experiments were conducted to measure the fluorescence intensity of MBP before and after addition of the FAsH dye. These results can be seen in Figure 7.2. As the plot shows, in the absence of dye, MBP in protein buffer showed very little fluorescence signal, as does the protein buffer without MBP. This confirmed that there was minimal fluorescence contribution from MBP and the protein buffer. However, upon addition of the FAsH dye, the fluorescence intensity increased by approximately five orders of magnitude. It should be noted that unbound FAsH dye in protein buffer alone does contribute to the overall fluorescence intensity. There is still a five-times increase in fluorescence intensity from unbound to bound FAsH dye.

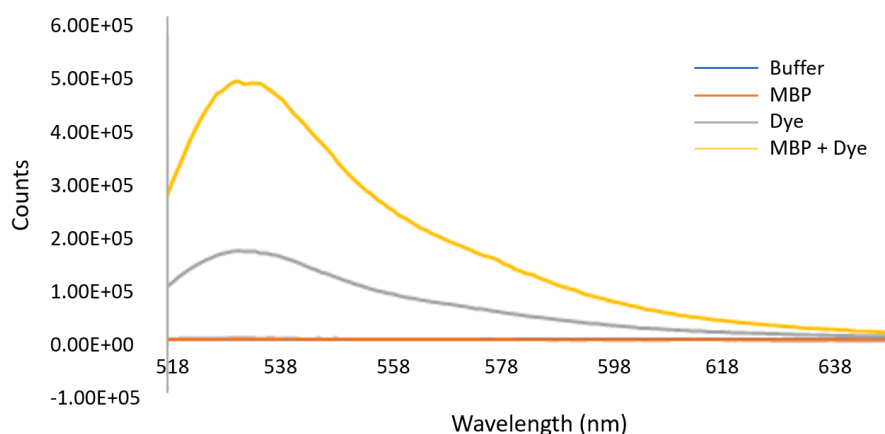


Figure 7.2 Fluorescence studies of maltose binding protein. After addition of the FAsH dye, the fluorescence intensity of MBP increased 5-fold, with little fluorescence observed prior to addition of the dye. Note that traces for the protein buffer and MBP alone overlap, both are indeed present in the plot.

### 7.3.2 Kinetic studies of dye binding

Fluorescence experiments were also done to study the kinetics of dye binding, the results of which are shown in Figure 7.3. The fluorescence intensity of MBP in the presence of FAsH dye was measured at different time points and was plotted as a function of time. As the amount of time the FAsH dye had to bind to the tetracysteine tag increased, so did the fluorescence intensity. Most of the FAsH dye appeared to bind almost instantaneously, with only a small increase in signal as time went on. The fluorescence intensity plateaued after approximately one hour had passed.

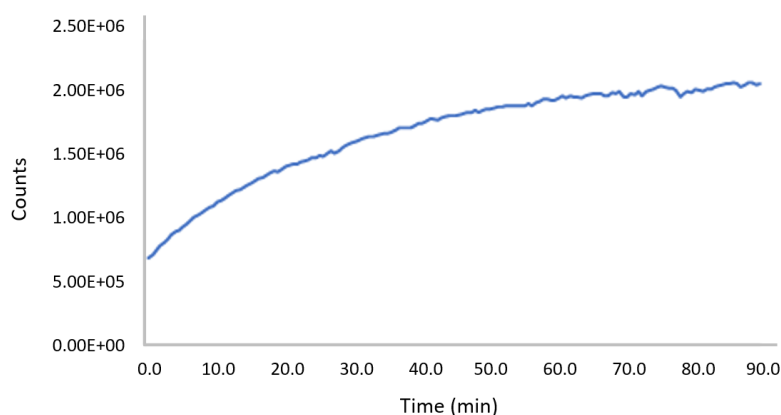


Figure 7.3 Kinetic studies of FAsH dye binding to a tetracysteine tag in MBP.

### 7.3.3 SHG imaging results

SHG images of the MBP-tetracysteine crystals were obtained before and after addition of the FAsH dye and are shown in Figure 7.4. Unfortunately, no SHG signal enhancement was observed. Despite multiple efforts to crystallize the MBP-TC construct and detect SHG after addition of the FAsH dye, an enhancement in SHG signal was unable to be measured. Additionally, when the SHG signal was measured after allowing the dye to bind overnight, there appeared to be a decrease in SHG. These findings suggest that the dye begins to degrade the quality of the crystals over time, leading to less SHG signal being detected. It is possible that this degradation was responsible for the lack of enhancement in SHG signal. For this reason, it was decided that use of the FAsH dye was not a viable option for improving the detection of protein crystals using SHG.

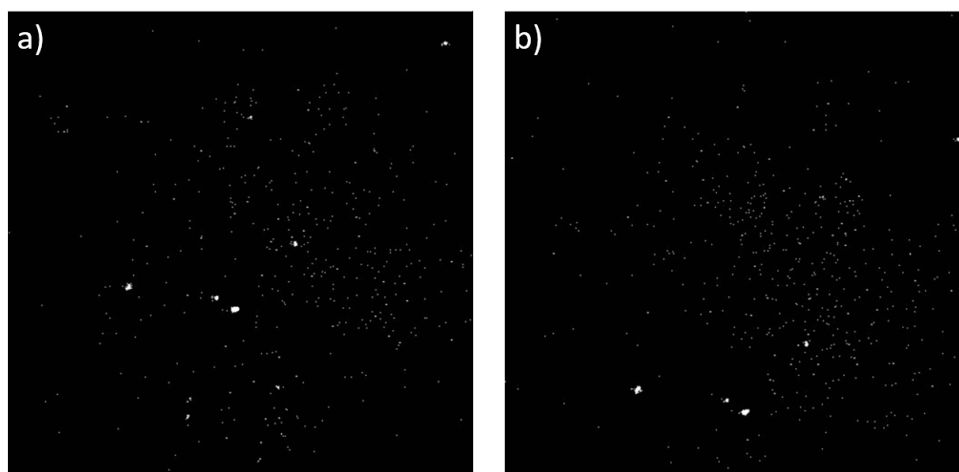


Figure 7.4 SHG images of MBP crystals before (a) and after (b) addition of 500 nM FAsH dye.

#### 7.4 Conclusions

While the successful incorporation of the tetracysteine tag into MBP was confirmed via fluorimetry measurements, measurements to determine the SHG enhancement upon addition of the FAsH dye were inconclusive. It appeared as though degradation of the crystals occurred after addition of the FAsH dye, suggesting that the addition of the tetracysteine tag had unintended adverse effects to the crystallization of the protein. This was further demonstrated by the difficulty in obtaining high quality crystals despite multiple crystallization trials. Further work can be done to investigate other alternatives for covalently bound dyes for SHG enhancement, such as use of a maleimide dye, which reacts specifically with sulfhydryl groups in proteins.

#### 7.5 References

1. Forsythe, S.; Achari, A.; Pusey, M.L. Trace fluorescent labeling for high-throughput crystallography. *Acta. Cryst. D.* **2006**, *62*, 339-346.
2. Madden, J.T., DeWalt, E.L., Simpson, G.J. Two-photon excited UV fluorescence for protein crystal detection. *Acta. Cryst. D.* **2011**, *67*, 839-846.
3. Vernede, X., Lavault, B., Ohana, J., Nurizzo, D., Joly, J., Jacquamet, L., Felisaz, F., Cipriani, F., Bourgeois, D. UV laser-excited fluorescence as a tool for the visualization of protein crystals mounted in loops. *Acta. Cryst. D.* **2006**, *62*, 253-261.
4. Desbois, S., Seabrook, S.A., Newman, J. Some practical guidelines for UV imaging in the protein crystallization laboratory. *Acta. Crystallogr. Sect. F. Struct. Biol. Cryst. Commun.* **2013**, *69*, 201-208.



5. Groves, M.R., Muller, I.B., Kreplin, X., Muller-Dieckman, J. A method for the general identification of protein crystals in crystallization experiments using a noncovalent fluorescent dye. *Acta. Cryst. D.* **2007**, *63*, 526-535.
6. Wampler, R.D.; Kissick, D.J.; Dehen, J.C.; Gualtieri, E.J.; Grey, J.L.; Wang, H.; Thompson, D.H.; Cheng, J.; Simpson, G.J. Selective detection of protein crystals by second harmonic generation. *J. Am. Chem. Soc.* **2008**, *130* (43), 14076-14077.
7. Newman, J.A., Scarborough, N.M., Pogranichniy, N.R., Shrestha, R.K., Closser, R.G., Das, C., Simpson, G.J. Intercalating dyes for enhanced contrast in second-harmonic generation imaging of protein crystals. *Acta. Cryst. D.* **2015**, *71*, 1471-1477.
8. Adams, S.R., Campbell, R.E., Gross, L.A., Martin, B.R., Walkup, G.K., Yao, Y., Llopis, J., Tsein, R.Y. New biarsenical ligands and tetracysteine motifs for protein labeling in vitro and in vivo: synthesis and biological applications. *J. Am. Chem. Soc.* **2002**, *124*, 6063-6076.
9. Rudner, L., Nydegger, S., Coren, L.V., Nagashima, K., Thali, M., Ott, D.E. Dynamic fluorescent imaging of human immunodeficiency virus type 1 gag in live cells by biarsenical labeling. *J. Virol.* **2005**, *79*, 4055-4065.
10. Fessenden, J.D., Mahalingam, M. Site-Specific Labeling of the Type 1 Ryanodine Receptor Using Biarsenical Fluorophores Targeted to Engineered Tetracysteine Motifs. *PLoS ONE* **2013**, *8*.
11. Waugh, D.S. Crystal structures of MBP fusion proteins. *Protein Science* **2016**, *25*, 559-571.

## **VITA**

Hilary M. Florian was born on October 9, 1992 in Washington, Pennsylvania to Glenn and Sandy Florian. She graduated from Trinity High School in 2011. She then followed in her brother Matthew's footsteps and attended Pennsylvania State University, where she obtained her B.S. in chemistry in 2015. After graduating from Penn State, she began her graduate career at Purdue University, working under Dr. Garth Simpson. Her thesis work focused on using nonlinear optical techniques to improve the detection and characterization of proteins as well as significant work at the Advanced Photon Source at Argonne National Laboratory.